Received: 24 June 2023 | Revised: 16 September 2023 | Accepted: 20 October 2023

DOI: 10.1002/nme.7398

RESEARCH ARTICLE

WILEY

Modeling cracks in viscoelastic materials at finite strains

Suhib Abu-Qbeitah | **Mahmood Jabareen** | **Konstantin Y. Volokh**

Faculty of Civil and Environmental Engineering, Technion - Israel Institute of Technology, Haifa, Israel

Correspondence
Mahmood Jabareen, Faculty of Civil and Environmental Engineering, Technion - Israel Institute of Technology, Haifa, Israel.
Email: cvjmah@technion.ac.il

Funding information
Israel Science Foundation, Grant/Award Number: ISF-394/20; Israeli Ministry of Science and Technology, Grant/Award Number: MOST-0005173; Neubauer Foundation

Abstract

Viscosity is a manifestation of internal friction in materials. Such friction is accompanied by the dissipation of energy, which affects deformation and fracture. In the present work, we develop a new theoretical formulation and its numerical implementation for modeling fracture in viscoelastic soft materials. Concerning the theory, we extend the material-sink approach by including a viscosity description at finite strains. Concerning numerical methods, we introduce a mixed finite-element formulation based on the relative deformation gradient and implement it in Abaqus. Representative numerical examples show that the proposed approach captures the viscous behavior of material and demonstrates the coupling between viscosity and fracture. Simulations reveal that the viscous dissipation suppresses minor crack branching as compared to the purely hyperelastic case, when the strain rate is relatively small. That said, when the strain rate is relatively large, viscoelastic and hyperelastic materials fracture consonantly.

KEYWORDS

Abaqus, large deformation, material-sink method, nonlinear viscoelasticity, rate-dependent fracture

1 | INTRODUCTION

Answering the questions of when and where the material fractures are of great necessity. Such questions can be addressed in experiments. However, acquiring data from experiments is costly, including multiple iterations, and, in some cases, physical experiments are simply hard to do. The experimental difficulties can be partly resolved by developing reliable theoretical and computational models to predict fracture: numerical simulations are cheaper than physical experiments and the iterating is easier. These models should describe real material behavior. In particular, regarding fracture, it was shown by Abu-Qbeitah et al.[1] that the onset of damage localization was followed by dynamic rather than quasi-static crack propagation. Thus, fracture should be studied via dynamic analysis that can describe the real unstable process starting once the crack initiates. Moreover, some materials are sensitive to the strain rate and exhibit a time-dependent response.[2,3] The rate-dependence can considerably affect their failure and fracture behavior.[*] Soft rate-dependent materials encompass pronounced physical and geometrical nonlinearities. Consequently, a nonlinear theory of viscoelasticity is needed to describe their real behavior while the linear viscoelasticity theory is, basically, inappropriate.[5]

Concerning history, we note that Griffith[6,7] pioneered criterion according to which a pre-existing crack becomes unstable when the balance between elastic and fracture energy is violated. In the case of viscoelastic materials, the consideration is subtler because additional energy is consumed in internal friction to form a new fracture surface.[8] The ability of some soft materials to dissipate the additional energy affects their toughness.[9] In terms of viscoelastic constitutive

models, a thorough review of rate-dependent (viscoelastic) fracture of polymers was presented by Knauss.[8] Persson and Brener[10] studied crack propagation in linear viscoelastic solids by calculating the dependence of the fracture energy on the crack velocity. Carbone and Persson[11] studied the influence of the temperature on the viscoelastic energy dissipation in rubber-like materials using a linear theory of viscoelasticity. They have found that a large increase in temperature could occur close to the crack tip that would extremely affect the viscoelastic energy dissipation around it.

More recent approaches to modeling fracture can be provisionally divided in the surface—cohesive zone models (CZM)—and the bulk—damage mechanics (DM)—ones. For example, Song et al.[12] studied viscoelastic fracture by using a bi-linear CZM, where cohesive elements were inserted over an area to allow the crack propagation. The use of CZM is justifiable when the crack path is known in advance, whereas, if the weak interface is not known beforehand then cohesive surfaces are inserted at the edges curbing the crack to propagate solely along prescribed paths. Such restriction may lead to overestimation of the dissipation energy if the true crack diverges from the restricted crack path, especially when the mesh is coarse. Moreover, using CZM one must define the traction-separation relationship across fracture surfaces, which induces artificial material anisotropy attributed to the usage of two different constitutive laws for the bulk and the fracture surface. A possible alternative to circumvent the deficiencies associated with the cohesive zone method is the extended finite element method (XFEM),[13-16] which was used by some researchers to model fracture in viscoelastic materials. Yu and Ren[17] and Ozupek and Iyidiker[18] modeled cracks in two-dimensional viscoelastic media using the XFEM, where enrichment functions for crack estimation in viscoelastic materials was defined. While the XFEM allows modeling cracks without the requirement of re-meshing, the generalization of theory to model cracks in three-dimensional solids is not trivial.

Examples of the bulk damage approaches include the so-called peridynamics and the element deletion approach. Mitchell[19] developed a non-local peridynamics viscoelasticity model, where the viscous effects was added to the deviatoric deformations. Madenci and Oterkus[3] developed a peridynamics model of viscoelastic materials in terms of Prony series tested on several benchmark examples, where they showed that their viscoelastic model captured the relaxation behavior of the material. However, since peridynamics uses meshless discretization, it leads to high computational costs, especially for three-dimensional simulations. The element deletion method is a practical method for modeling fracture in which the elements that satisfy the deletion criterion are dropped from the further analysis. Although the latter approach is simple, Song et al.[14] showed that the crack path was sensitive to mesh refinement and the crack speed was substantially underestimated. Later on, Thamburaja et al.[20] showed that the mesh sensitivity shortcoming could be mitigated by using a thermodynamically-consistent non-local fracture criterion.

Recently, bulk damage approaches called phase-field methods gained popularity as a tool to simulate cracks[21] and they were adapted for viscoelastic materials. Miehe et al.[22] introduced a viscosity parameter in the phase-field modeling of fracture. However, the viscosity assumed for the evolution of the phase-field was solely numerically motivated[21]—it was used as an artificial feature that stabilized the simulation. Shen et al.[23] proposed a new phase-field theory to study the fracture behavior of viscoelastic solids in the small strain context and concluded that at low strain rates the viscous dissipation did not affect the crack propagation path, while it accelerated the crack growth rate. On the other hand, at high strain rates, the effect of viscous dissipation on the fracture growth rate and crack path was marginal. Loew et al.[24] developed a phase-field model to predict rate-dependent fracture of rubber, where Loew et al.[24] extended Miehe and Schanzel[25] model to depend on time and the loading rate. Yin et al.[26] proposed a modified form of a phase-field approach by incorporating a strain rate-dependent fracture toughness, which led to the relationship: the faster the loading the higher the strength. Brighenti et al.[27] studied the strain rate behavior of polymers by adopting a micromechanical model rather than a phenomenological one. Their formulation was scaled to the continuum domain and combined with the phase-field to simulate fracture of polymers. Dammas et al.[21] proposed a unified phase-field to model fracture of viscoelastic solids. While the latter formulation is thermodynamically consistent, it is restricted by small strain settings and the inertia effects are neglected.

Although various phase-field methods offer a simple way to simulate cracks with complex topologies, there are claims in the literature that when the characteristic length of the diffused damage area approaches zero, the fundamental theory of Griffith is recovered.[21] This may lead to the assumption that the characteristic length is a numerical parameter that should be chosen small enough. However, a significant influence of the characteristic length on the results was observed by Zhang et al.[28] Thus, these claims are debatable and the characteristic length should be a fixed material parameter.[29-34] A somewhat simple discussion of the meaning of the characteristic length in the phase-field models can be found in Reference 7.

While most methods of modeling bulk damage rely on the purely mathematical regularization techniques, Volokh[35] proposed the material-sink (MS) approach stemming from the physical observation of the diffused bond breakage. Such breakage leads to the local material loss and the mass is not preserved within a small volume of the localized damage. Thus, the mass density decreases and activates the mass balance law as an additional one to the momenta balance.

Consequently, the whole fracture process is encapsulated in two balance laws. Obviously, MS method does not require numerical tracking of discontinuities in the displacement field and it can model cracks that are not known in advance. Due to its simplicity, MS approach can be easily implemented in the existing commercial finite element softwares. For instance, it was implemented by Anshul et al.[36] in the finite element software FEAP to study the effect of inertia on the dynamic fracture process.[36] Abu-Qbeitah et al.[1,37] further modified the MS approach for static and dynamic fracture simulations to fit the Abaqus software.

The present work couples a nonlinear viscoelasticity theory with the MS approach. Therefore, the main objective of the present study is to develop a computational model based on the material sink approach that can predict fracture in nonlinear viscoelastic materials. By harnessing a nonlinear viscoelasticity theory coupled with the MS model of fracture, the fracture mechanisms of materials under large deformation in a rate-dependent setting can be simulated. Also, the developed formulation is implemented into the FEM software Abaqus/Standard 2020[38] via a user-defined element subroutine (UEL) interface, which allows studying the crack propagation and the failure mechanism in nonlinear viscoelastic materials.

The article is structured as follows. The basic equations of the MS method coupled with a nonlinear theory of viscoelasticity are introduced in Section 2, in which the integration of the viscoelastic constitutive equations is also outlined. A mixed finite element formulation, based on the relative deformation gradient, is presented in Section 3, where the way to overcome the locking behavior for nearly incompressible materials is also discussed. Several numerical examples, including two- and three-dimensional cases, are studied in Section 4. Finally, the overall arguments and findings are summarized in Section 5.

2 | THEORETICAL BACKGROUND OF THE MATERIAL-SINK APPROACH IN A RATE-DEPENDENT SETTING

In the case of fracturing concrete, the dust and small pieces of material coming out of cracks can be observed by a naked eye. In the case of polymers, the debris cannot be seen by the naked eye yet the new experimental techniques (cf. Slootman et al.[39]) can catch the diffused bond breakage visually. In other words, when the material fractures (i.e., damage develops into cracks), the mass is not preserved anymore, and the mass conservation law should be replaced by the mass balance.[35] The latter law couples with momenta balance to produce solution of the crack propagation problem. The mass balance law naturally regularizes computations suppressing the pathological mesh-dependence and zero energy fracture. Eventually, the mass density becomes a variable that decreases in the place where the damage localizes, indicating the crack propagation path. In this section, a rate-dependent formulation of the coupled boundary value problem is proposed by merging a nonlinear viscoelastic constitutive model with the MS theory.

2.1 | Balance equations

Equations of the mass and linear momentum balance can be written in the following forms,[35] respectively,

$$\begin{aligned} \operatorname{div}(\mathbf{s}) + \xi &= 0, \\ \operatorname{div}(\boldsymbol{\sigma}) - \varrho\dot{\mathbf{v}} &= \mathbf{0}, \end{aligned} \tag{1}$$

where $\mathbf{s}$ is the Eulerian mass flux, ξ is the Eulerian mass source (sink), $\boldsymbol{\sigma}$ is the Cauchy stress, ϱ is the Eulerian mass density, and $\mathbf{v}$ is the velocity vector. The body forces in the linear momentum balance equation are ignored. Also, it is assumed that the bond rupture is so fast (at the pico-second scale) that we can ignore the dynamic process of the transition from the intact to ruptured molecular/atomic bonds. The latter assumption mathematically means that we can drop the density rate terms. In addition, damage is highly localized, so the linear momentum balance (i.e., $(1)_2$) can be written in the standard form without considering momenta due to the mass alterations resulting from crack propagation.

To complete the formulation of the initial-boundary value problem, proper boundary conditions should be set. The natural or Neumann boundary conditions implying mass balance and momentum balance on the boundary are given below by $(2)_1$ and $(2)_3$, respectively. Alternatively, the essential or Dirichlet boundary conditions are given by $(2)_2$ and $(2)_4$ as follows

$$\begin{aligned} \mathbf{s}\cdot\mathbf{n} = 0 \ \text{ on } \ \Gamma^s \quad \text{and} \quad \varrho = \overline{\varrho} \ \text{ on } \ \Gamma^{\varrho}, \\ \boldsymbol{\sigma}\mathbf{n} = \bar{\mathbf{t}} \ \text{ on } \ \Gamma^t \quad \text{and} \quad \mathbf{u} = \overline{\mathbf{u}} \ \text{ on } \ \Gamma^u, \end{aligned} \tag{2}$$

where $\mathbf{n}$ is a unit outward normal to the boundary in the current configuration, $\bar{\varrho}$ is the prescribed mass density applied on the boundary Γ^{ϱ}, $\bar{\mathbf{t}}$ is the given traction applied on the boundary Γ^{t}, and $\bar{\mathbf{u}}$ is the prescribed displacement applied on the boundary Γ^{u}. Initial conditions in the initial configuration $\mathcal{B}_0$ complete the formulation of the coupled mass-flow-elastic initial boundary value problem

$$\mathbf{u}(t=0)=\mathbf{u}_0, \quad \mathbf{v}(t=0)=\mathbf{v}_0, \quad \varrho(t=0)=\varrho_0, \tag{3}$$

where $\mathbf{u}_0$, $\mathbf{v}_0$, and ϱ_0 are the initial displacement, velocity, and mass density, respectively.

We note in passing that the boundary condition $(2)_2$ is hardly necessary practically.

2.2 | Constitutive equations

The behavior of viscoelastic material can be represented using conceptual models consisting of springs and dashpots, corresponding respectively to elastic and viscous elements. These models provide physical intuition and have scholastic significance as well. In the present work, the standard solid model is adopted, in which a Maxwell[†] model is connected to a spring in parallel, as shown in the circle in Figure 1. It is worth noting that the Maxwell model exhibits unlimited creep, wherefore it is also called Maxwell fluid.[40] For this reason, the addition of a spring to the Maxwell model stabilizes the model, making it able to describe the physical behavior of solids. It shall be noted that the branches can be more than two, that is, one equilibrium and several non-equilibrium branches. However, in the present work, we use a simplification of only one equilibrium and one non-equilibrium branches. The generalization of the viscoelastic model to a number of dashpot-spring elements is presented in Appendix C.

For the adopted viscoelastic rheological model[‡] (as shown in the circle in Figure 1), the Cauchy stress splits as follows

$$\boldsymbol{\sigma}=\boldsymbol{\sigma}_{\mathrm{A}}+\boldsymbol{\sigma}_{\mathrm{B}}. \tag{4}$$

Here, it is assumed that the deformation in spring A is described by the total left Cauchy–Green tensor $\mathbf{b}=\mathbf{F}\mathbf{F}^{\mathrm{T}}$, the deformation in spring B is described by the deformation tensor $\mathbf{b}_{\mathrm{B}}=\mathbf{b}_{\mathrm{B}}^{\mathrm{T}}$, and the deformation rate in the dashpot is described by tensor $\mathbf{d}_{\mathrm{B}}=\mathbf{d}_{\mathrm{B}}^{\mathrm{T}}$. In particular, the evolution equation of the total left Cauchy–Green tensor reads

$$\dot{\mathbf{b}}=\mathbf{l}\mathbf{b}+\mathbf{b}\mathbf{l}^{\mathrm{T}}, \tag{5}$$

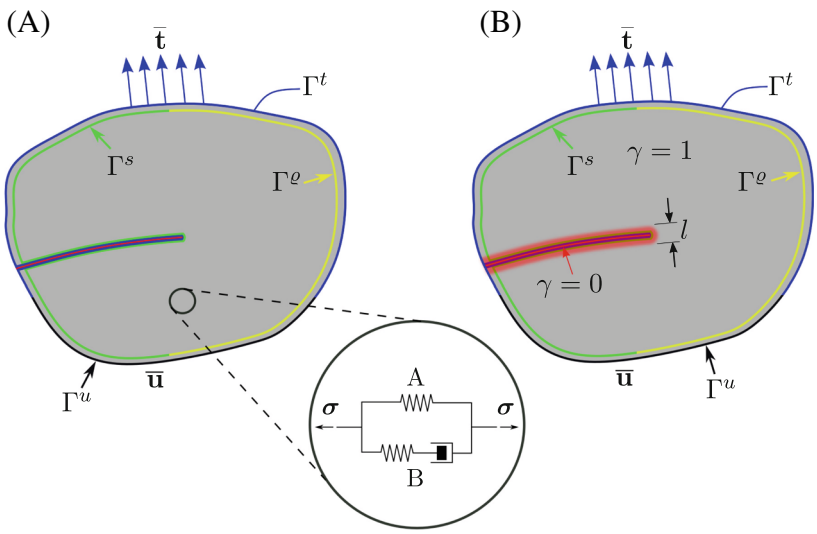

FIGURE 1 Schematic drawing of a domain with a crack: (A) Discrete representation of the crack, and (B) regularized representation by the relative density scalar field γ. The characteristic length l governs the width of the regularized crack. The viscoelastic rheological model is shown in the middle circle.

with the initial condition $\mathbf{b}(t=0)=\mathbf{I}$. Following the work of Volokh[5] and Aranda-Iglesias et al.,[41] the evolution equation of the deformation tensor $\mathbf{b}_{\mathrm{B}}$ is given by

$$\dot{\mathbf{b}}_{\mathrm{B}} = (\mathbf{l}-\mathbf{d}_{\mathrm{B}})\mathbf{b}_{\mathrm{B}} + \mathbf{b}_{\mathrm{B}}(\mathbf{l}-\mathbf{d}_{\mathrm{B}})^{\mathrm{T}}, \tag{6}$$

where $\mathbf{l}=\mathrm{grad}(\mathbf{v})$ is the velocity gradient and the initial condition $\mathbf{b}_{\mathrm{B}}(t=0)=\mathbf{I}$. Further, the Helmholtz free energy per unit mass w is defined as follows

$$w(\mathbf{b},\mathbf{b}_{\mathrm{B}}) = w_{\mathrm{A}}(\mathbf{b}) + w_{\mathrm{B}}(\mathbf{b}_{\mathrm{B}}). \tag{7}$$

In this contribution, we ignore thermal processes and we use the dissipation inequality in the reduced form

$$D_{\mathrm{int}} = \boldsymbol{\sigma} : \mathbf{d} - \varrho\dot{w} - \dot{\varrho}w \geq 0, \tag{8}$$

where $\dot{\varrho}w$ term is negligible based on the assumption that mass density changes in time as a step function due to the fast fracture process as we discussed previously. In (8), $\mathbf{d}=(\mathbf{l}+\mathbf{l}^{\mathrm{T}})/2$ is the deformation rate tensor.

Substituting the time derivative of the strain energy function (7) into the dissipation inequality (8), using the evolution Equations (5) and (6), and noting the symmetry feature

$$\frac{\partial w_{\mathrm{A}}}{\partial \mathbf{b}}\mathbf{b} = \mathbf{b}\frac{\partial w_{\mathrm{A}}}{\partial \mathbf{b}}, \quad \frac{\partial w_{\mathrm{B}}}{\partial \mathbf{b}_{\mathrm{B}}}\mathbf{b}_{\mathrm{B}} = \mathbf{b}_{\mathrm{B}}\frac{\partial w_{\mathrm{B}}}{\partial \mathbf{b}_{\mathrm{B}}}, \tag{9}$$

the constitutive laws for springs A and B are, respectively, given by

$$\boldsymbol{\sigma}_{\mathrm{A}} = 2\varrho\frac{\partial w_{\mathrm{A}}}{\partial \mathbf{b}}\mathbf{b}, \quad \boldsymbol{\sigma}_{\mathrm{B}} = 2\varrho\frac{\partial w_{\mathrm{B}}}{\partial \mathbf{b}_{\mathrm{B}}}\mathbf{b}_{\mathrm{B}}, \tag{10}$$

and the dissipation inequality reduces to

$$D_{\mathrm{int}} = \boldsymbol{\sigma}_{\mathrm{B}} : \mathbf{d}_{\mathrm{B}} \geq 0. \tag{11}$$

Constitutive laws for the mass flux and mass source are defined in the following forms, respectively,

$$\mathbf{s} = \kappa I_3^{-1/2}\mathbf{b}\ \mathrm{grad}\left(I_3^{1/2}\varrho\right), \quad \xi = \beta\varrho_0 - \frac{\beta\varrho I_3^{1/2}}{\exp\left[-(w_{\mathrm{A}}/\phi_{\mathrm{A}})^m\right]}, \tag{12}$$

where $\varrho_0=\varrho(t=0)$; $\beta>0$ and $\kappa>0$ are material constants; $I_3=\det(\mathbf{b})$, ϕ_{A} is the energy limiter per unit mass, which is calibrated in macroscopic experiments (it is a material parameter that controls the critical failure energy indicating the maximum strain energy that the material can sustain, implying the onset of material instability), m is a dimensionless material parameter, which controls the sharpness of the transition to material damage on the stress-strain curve. Note that the exponent of the mass source term depends on the strain energy and the energy limiter values on the spring A, where there is no need to limit the energy of spring B as long as the failure of spring A leads to the overall failure.

Remark 1. The particular form of the constitutive law for the mass sink is a subtle matter that can be explained as follows. The material volume has a finite number of particles, implying the energy of their bonds is finite. The latter means that the strain energy should be bounded, which implies bounded stresses. The latter observation was formulated by Volokh[4,5,42,43] via the energy limiter approach, in which ϕ is the average bond energy. Now, the underlying concept of adopting this particular form of the constitutive law for the mass source/sink is that prior damage—failure—the theory reduces to the energy limiter approach that limits the strain energy, indicating the onset of material damage. For further information, interested readers are referred to Reference 37.

Substituting of $(12)_1$ and $(12)_2$ in $(1)_1$ and dividing by $\beta\varrho_0$ we obtain

$$\mathrm{div}(\mathbf{f}) + \zeta = 0, \tag{13}$$

where the vector $\mathbf{f}$ and the scalar ζ are defined as follows

$$\mathbf{f} = l^2 I_3^{-1/2}\mathbf{b}\,\mathrm{grad}\left(I_3^{1/2}\gamma\right), \quad \zeta = 1 - \frac{\gamma I_3^{1/2}}{\exp\left[-(W_\mathrm{A}/\Phi_\mathrm{A})^m\right]}, \tag{14}$$

where the parameter $l = \sqrt{\kappa/\beta}$ is the characteristic length of the material. It is noticed from (14) that the scalars κ and β are not required as the characteristic length replaces them. On the other hand, in (14) the dimensionless (or relative) mass density γ replaces the mass density ϱ, the Helmholtz free energy per unit referential volume W_A replaces the Helmholtz free energy per unit mass w_A, and the energy limiter (or the average bond energy) per unit referential volume Φ_A replaces the energy limiter per unit mass ϕ_A using the following relations

$$\gamma = \frac{\varrho}{\varrho_0}, \quad W_\mathrm{A} = \varrho_0 w_\mathrm{A}, \quad \Phi_\mathrm{A} = \varrho_0\phi_\mathrm{A}. \tag{15}$$

It is worth noting that the characteristic length (l) controls the width of the diffused crack. It is a material parameter calibrated via experiments to match the considered material's strength. Furthermore, the relative mass density γ was used to represent fracture instead of the mass density ϱ. Using the relative density is preferable since it is a dimensionless quantity that has values between 0 and 1. Figure 1 illustrates the regularization scheme using the MS theory, where the crack surfaces in Figure 1A are presented with the diffused damaged zone in Figure 1B using the relative mass density scalar γ, with values ranging from 0 to 1. The former value means that the material is fully fractured, while the latter value means that the material is fully intact. That is to say, the relative density approaches zero at the center of the diffused damage and approaches unity away from the center. It is convenient to modify the scalar $\zeta(14)_2$ in order to enforce the irreversibility of the damage via a history variable $\mathcal{H}$. The history variable is used to ensure the local crack driving force is non-decreasing ($\dot{\gamma} \leq 0$) in computations. Thus, ζ is rewritten as

$$\zeta = 1 - \frac{\gamma I_3^{1/2}}{\mathcal{H} + \varepsilon}, \tag{16}$$

in which $0 < \varepsilon \ll 1$ is a dimensionless constant that serves to avoid numerical singularity when $\mathcal{H}$ approaches zero. From the numerical point of view, the constant ε was set to 10^{-15}. The history variable $\mathcal{H}$ is given by

$$\mathcal{H}(t_0) = 1, \quad \mathcal{H}(t_{n+1}) = \min\begin{Bmatrix}\exp\left[-(W_\mathrm{A}/\Phi_\mathrm{A})^m\right] \\ \mathcal{H}(t_n)\end{Bmatrix}. \tag{17}$$

The constitutive equations that govern the Cauchy stress of isotropic hyperelastic material can be written in the canonical forms accordingly

$$\begin{aligned}\boldsymbol{\sigma}_\mathrm{A} &= 2\gamma\frac{\partial W_\mathrm{A}}{\partial \mathbf{b}}\mathbf{b} = 2\gamma(I_3 W_{\mathrm{A}3}\mathbf{I} + (W_{\mathrm{A}1} + I_1 W_{\mathrm{A}2})\mathbf{b} - W_{\mathrm{A}2}\mathbf{b}^2),\\ \boldsymbol{\sigma}_\mathrm{B} &= 2\gamma\frac{\partial W_\mathrm{B}}{\partial \mathbf{b}_\mathrm{B}}\mathbf{b}_\mathrm{B} = 2\gamma(I_{\mathrm{B}3} W_{\mathrm{B}3}\mathbf{I} + (W_{\mathrm{B}1} + I_{\mathrm{B}1} W_{\mathrm{B}2})\mathbf{b}_\mathrm{B} - W_{\mathrm{B}2}\mathbf{b}_\mathrm{B}^2),\end{aligned} \tag{18}$$

where $I_1 = \mathrm{tr}\mathbf{b}$, $2I_2 = (\mathrm{tr}\mathbf{b})^2 - \mathrm{tr}(\mathbf{b}^2)$, $I_3 = \det\mathbf{b}$ are the invariants of the total left Cauchy–Green deformation tensor, while $I_{\mathrm{B}1} = \mathrm{tr}\mathbf{b}_\mathrm{B}$, $2I_{\mathrm{B}2} = (\mathrm{tr}\mathbf{b}_\mathrm{B})^2 - \mathrm{tr}(\mathbf{b}_\mathrm{B}^2)$, and $I_{\mathrm{B}3} = \det\mathbf{b}_\mathrm{B}$ are the invariants of the deformation tensor associated with spring B. Also, functions $W_{\mathrm{A}i} = \partial W_\mathrm{A}/\partial I_i$ are the derivatives of the strain energy density associated with spring A (i.e., W_A), while functions $W_{\mathrm{B}i} = \partial W_\mathrm{B}/\partial I_{\mathrm{B}i}$ are the derivatives of the strain energy density associated with spring B (i.e., W_B). It is worth noting that $(18)_1$ and $(18)_2$ represent hyperelastic constitutive equations in the case where material density varies according to the mass balance equation $(1)_1$.

Finally, the flow rule for the dashpot in the rheological model is defined as a generalized Reiner–Rivlin model

$$\boldsymbol{\sigma}_\mathrm{B} = \beta_1\mathbf{I} + \beta_2\mathbf{d}_\mathrm{B} + \beta_3\mathbf{d}_\mathrm{B}^2, \tag{19}$$

where β_js are the function(al)s, generally, depending on stresses. Substituting (19) in (11), the reduced dissipation inequality becomes

$$D_\mathrm{int} = \beta_1\mathrm{tr}\mathbf{d}_\mathrm{B} + \beta_2\mathrm{tr}\mathbf{d}_\mathrm{B}^2 + \beta_3\mathrm{tr}\mathbf{d}_\mathrm{B}^3 \geq 0. \tag{20}$$

For a wide class of materials, it is possible to postulate that $\beta_3 = 0$ (cf. Volokh[5]). Also, taking into account the incompressibility condition ($\mathrm{tr}\mathbf{d}_\mathrm{B} = 0$), it can be shown that the coefficient β_1 and the tensor $\mathbf{d}_\mathrm{B}$ are given by

$$\beta_1 = \frac{1}{3}\mathrm{tr}\boldsymbol{\sigma}_\mathrm{B}, \quad \mathbf{d}_\mathrm{B} = \frac{1}{\beta_2}\mathrm{dev}\boldsymbol{\sigma}_\mathrm{B}, \tag{21}$$

and reduced form of the dissipation inequality (11) becomes

$$D_\mathrm{int} = \beta_2 \mathrm{tr}\mathbf{d}_\mathrm{B}^2 \geq 0, \tag{22}$$

which can be fulfilled by imposing the following restriction on the viscosity parameter

$$\beta_2 > 0. \tag{23}$$

It can be noticed that the proposed formulation creates coupling between fracture and viscosity. On the one hand, the values of the displacements are dependent on the relative mass density variable, through the Cauchy stress (i.e., (18)) and through the mass matrix as will be shown in (49). On the other hand, the value of the relative mass density is dependent, through the mass source and sink terms (14), on the total left Cauchy–Green deformation tensor.

2.3 | Integration of the evolution equations

The evolution Equation (5) of the total left Cauchy–Green deformation tensor and the evolution Equation (6) of the deformation tensor $\mathbf{b}_\mathrm{B}$ require algorithms to update all variables given at time t_n for time t_{n+1}. To this end, the relative deformation gradient that maps a material point from the configuration at time t_n to the time t_{n+1} is defined as follows

$$\mathbf{F}_r = \frac{\partial \mathbf{x}}{\partial \mathbf{x}^n}, \quad \dot{\mathbf{F}}_r = \frac{\partial \mathbf{v}}{\partial \mathbf{x}^n} = \mathbf{l}\mathbf{F}_r. \tag{24}$$

The values of the relative deformation gradient at times t_{n+1} and t_n are, respectively, given by

$$\mathbf{F}_r^{n+1} = \mathbf{F}^{n+1}(\mathbf{F}^n)^{-1}, \quad \mathbf{F}_r^n = \mathbf{I}, \tag{25}$$

where superscripts n and $n+1$ denote variables at times t_n and t_{n+1} accordingly: $(\bullet)^n \equiv (\bullet)(t_n)$ and $(\bullet)^{n+1} \equiv (\bullet)(t_{n+1})$. It can be shown that the exact solution of the evolution Equation (5) reads

$$\mathbf{b} = \mathbf{F}_r \mathbf{b}^n \mathbf{F}_r^\mathrm{T}, \tag{26}$$

and the value of the total deformation tensor $\mathbf{b}$ at time t_{n+1} is given by

$$\mathbf{b}^{n+1} = \mathbf{F}_r^{n+1}\mathbf{b}^n\left(\mathbf{F}_r^{n+1}\right)^\mathrm{T}. \tag{27}$$

The idea of the integration algorithm of (6) comes from the notion that the Oldroyd objective rate $\overset{\diamond}{\mathbf{b}}_\mathrm{B}$ can be written with respect to *arbitrary* reference configuration $\mathbf{x}^n$ in the following form

$$\overset{\diamond}{\mathbf{b}}_\mathrm{B} \equiv \dot{\mathbf{b}}_\mathrm{B} - \mathbf{l}\mathbf{b}_\mathrm{B} - \mathbf{b}_\mathrm{B}\mathbf{l}^\mathrm{T} = \mathbf{F}_r \partial(\mathbf{F}_r^{-1}\mathbf{b}_\mathrm{B}\mathbf{F}_r^{-\mathrm{T}})/\partial t \mathbf{F}_r^\mathrm{T}, \tag{28}$$

Substitution of (28) in (6) and taking into account the coaxiality between the tensors $\mathbf{b}_\mathrm{B}$ and $\mathbf{d}_\mathrm{B}$ (i.e., $\mathbf{d}_\mathrm{B}\mathbf{b}_\mathrm{B} = \mathbf{b}_\mathrm{B}\mathbf{d}_\mathrm{B}$) yield

$$\frac{\partial(\mathbf{F}_r^{-1}\mathbf{b}_\mathrm{B}\mathbf{F}_r^{-\mathrm{T}})}{\partial t} = -2\mathbf{F}_r^{-1}\mathbf{d}_\mathrm{B}\mathbf{b}_\mathrm{B}\mathbf{F}_r^{-\mathrm{T}}. \tag{29}$$

Equation (29) can be discretized with respect to time by employing either the forward Euler scheme (that is, the explicit scheme) or the backward Euler scheme (that is, the implicit scheme). Specifically, using the forward Euler scheme of the time derivative on interval $[t_n, t_{n+1}]$, the temporal discretization of (29) reads

$$(\mathbf{F}_r^{n+1})^{-1}\mathbf{b}_{\mathrm{B}}^{n+1}(\mathbf{F}_r^{n+1})^{-\mathrm{T}} = (\mathbf{F}_r^{n})^{-1}\mathbf{b}_{\mathrm{B}}^{n}(\mathbf{F}_r^{n})^{-\mathrm{T}} - 2\Delta t\ (\mathbf{F}_r^{n})^{-1}\mathbf{d}_{\mathrm{B}}^{n}\mathbf{b}_{\mathrm{B}}^{n}(\mathbf{F}_r^{n})^{-\mathrm{T}}, \tag{30}$$

with $\Delta t = t_{n+1} - t_n$. Substitution of $(25)_2$ in (30) yields

$$\mathbf{b}_{\mathrm{B}}^{n+1} = \mathbf{F}_r^{n+1}\left[\mathbf{I} - 2\Delta t\mathbf{d}_{\mathrm{B}}^{n}\right]\mathbf{b}_{\mathrm{B}}^{n}(\mathbf{F}_r^{n+1})^{\mathrm{T}}. \tag{31}$$

However, using the backward Euler scheme of the time derivative on interval $[t_n, t_{n+1}]$, the temporal discretization of (29) reads

$$(\mathbf{F}_r^{n+1})^{-1}\mathbf{b}_{\mathrm{B}}^{n+1}(\mathbf{F}_r^{n+1})^{-\mathrm{T}} = (\mathbf{F}_r^{n})^{-1}\mathbf{b}_{\mathrm{B}}^{n}(\mathbf{F}_r^{n})^{-\mathrm{T}} - 2\Delta t\ (\mathbf{F}_r^{n+1})^{-1}\mathbf{d}_{\mathrm{B}}^{n+1}\mathbf{b}_{\mathrm{B}}^{n+1}(\mathbf{F}_r^{n+1})^{-\mathrm{T}}. \tag{32}$$

Using $(25)_2$, (32) becomes

$$\mathbf{b}_{\mathrm{B}}^{n+1} = \left[\mathbf{I} + 2\Delta t\ \mathbf{d}_{\mathrm{B}}^{n+1}\right]^{-1}\underbrace{\mathbf{F}_r^{n+1}\mathbf{b}_{\mathrm{B}}^{n}(\mathbf{F}_r^{n+1})^{\mathrm{T}}}_{\text{elastic trial}}, \tag{33}$$

where $\mathbf{F}_r^{n+1}\mathbf{b}_{\mathrm{B}}^{n}(\mathbf{F}_r^{n+1})^{\mathrm{T}}$ is called the elastic trial. Since the deformation rate in the dashpot $\mathbf{d}_{\mathrm{B}}^{n+1}$ depends on $\mathbf{b}_{\mathrm{B}}^{n+1}$, (33) is implicit and its solution can be iteratively obtained. The iterative procedure for determining $\mathbf{b}_{\mathrm{B}}^{n+1}$ is described in the following flow chart:

1. At the first iteration, assume that the value of $\mathbf{d}_{\mathrm{B}}^{n+1}$ is
$$\mathbf{d}_{\mathrm{B}}^{n+1} = \mathbf{d}_{\mathrm{B}}^{n}.$$
2. Calculate the deformation tensor $\mathbf{b}_{\mathrm{B}}^{n+1}$ using (33)
$$\mathbf{b}_{\mathrm{B}}^{n+1} = \left[\mathbf{I} + 2\Delta t\ \mathbf{d}_{\mathrm{B}}^{n+1}\right]^{-1}\mathbf{F}_r^{n+1}\mathbf{b}_{\mathrm{B}}^{n}\left(\mathbf{F}_r^{n+1}\right)^{\mathrm{T}}.$$
3. Based on $\mathbf{b}_{\mathrm{B}}^{n+1}$ calculate the stress tensor $\boldsymbol{\sigma}_{\mathrm{B}}^{n+1}$ associated with the spring B using $(18)_2$
4. Update the deformation rate in the dashpot $\mathbf{d}_{\mathrm{B}}^{n+1}$ using $(21)_2$
$$\mathbf{d}_{\mathrm{B}}^{n+1} = \frac{1}{\beta_2}\mathrm{dev}\boldsymbol{\sigma}_{\mathrm{B}}^{n+1}.$$
5. Repeat steps 2–4 until convergence

It may be observed that the explicit scheme is simple to use and is computationally less demanding compared to the implicit scheme. Thus, in all of the examples in this study, the explicit scheme is adopted. That said, in the numerical experiments section, one example is solved using both schemes and results are compared.

3 | FINITE-ELEMENT FORMULATION

The standard finite-element approach suffers from volumetric locking when modeling nearly and fully incompressible materials.[44] In this case, reliable results using the standard finite elements cannot be obtained. Alternative approaches can be used to overcome the volumetric locking pathology. One of these methods is the reduced mixed finite element formulation,[45,46] which is a simple, yet, robust approach and its implementation requires only modifying the quantities obtained from the standard finite-element approach. On the other hand, Weickenmeier and Jabareen[47] developed a mixed

finite element formulation based on the relative deformation gradient, which is the appropriate kinematic measure for the viscoelastic theory adopted in the present work. Using the relative deformation gradient as the deformation measure implies that the reference configuration turns out to be unimportant and all calculations are conducted on the deformed configurations at times t_n and t_{n+1}. It is worth mentioning that to make the derivation as neat as possible, any quantity with the superscript n implies that the quantity is calculated at time t_n. On the other hand, any quantity without the superscript n implies that the quantity is calculated at time t_{n+1}.

For the forthcoming derivations, the weak form of the governing equations (1) is additively decomposed into two parts, where the first part is associated with the weak form of the balance of linear momentum, while the second part is associated with the weak form of the mass balance

$$\delta\Pi = \delta\Pi^u + \delta\Pi^\gamma = \sum_{e=1}^{N_{\text{el}}} \left(\delta\Pi_e^u + \delta\Pi_e^\gamma\right) = 0, \tag{34}$$

where N_{el} is the number of elements in the domain.

3.1 | Momentum balance

The weak form of the balance of linear momentum is formulated using the Hu–Washizu principle and written with respect to three independent fields, which are the modified relative deformation gradient $\widetilde{\mathbf{F}}_r$, the assumed relative dilatation measure $\overline{J}_r$, and the assumed hydrostatic pressure $\overline{p}$. This weak form is given by

$$\delta\Pi_e^u = \int_{\Omega_e} \varrho\ddot{\mathbf{u}} \cdot \delta\mathbf{u}\, d\Omega_e + \int_{\Omega_e^n} \left[\frac{1}{J^n}\widetilde{\mathbf{P}} : \delta\widetilde{\mathbf{F}} + \delta\overline{p}\left(J_r - \overline{J}_r\right) + \overline{p}\left(\delta J_r - \delta\overline{J}_r\right)\right] d\Omega_e^n - \delta\Pi_e^{u,\text{ext}}, \tag{35}$$

where $\ddot{\mathbf{u}}$ is the acceleration field, $\delta\mathbf{u}$ is the virtual displacement field, Ω_e is the element domain at the time t_{n+1}, Ω_e^n is the element domain at time t_n, $J^n = \det\left(\mathbf{F}^n\right)$ is the determinant of the deformation gradient at time t_n, $\widetilde{\mathbf{F}}$ is the modified deformation gradient tensor, $\widetilde{\mathbf{P}} = \frac{\partial W}{\partial \mathbf{F}}|_{\mathbf{F}=\widetilde{\mathbf{F}}}$ is the modified first Piola-Kirchhoff stress tensor, $\overline{p}$ is a scalar related to hydrostatic pressure, $J_r = \det(\mathbf{F}_r)$ is the determinant of the relative deformation gradient tensor, $\overline{J}_r$ is a scalar related to the relative volumetric dilatation, and $\delta\Pi_e^{u,\text{ext}}$ is the virtual work due to external forces. The modified deformation gradient $\widetilde{\mathbf{F}}$ can be decomposed into a modified relative deformation gradient (i.e., $\widetilde{\mathbf{F}}_r$) and a modified deformation gradient at time t_n (i.e., $\widetilde{\mathbf{F}}^n$) as follows

$$\widetilde{\mathbf{F}} = \widetilde{\mathbf{F}}_r\widetilde{\mathbf{F}}^n, \quad \widetilde{\mathbf{F}}_r = \left(\frac{\overline{J}_r}{J_r}\right)^{1/3}\mathbf{F}_r, \quad \widetilde{\mathbf{F}}^n = \left(\frac{\overline{J}^n}{J^n}\right)^{1/3}\mathbf{F}^n, \tag{36}$$

where $\overline{J}^n$ is a scalar related to the volumetric dilatation at time t_n. Following the work of Weickenmeier and Jabareen,[47] the weak form of the balance of linear momentum is written as

$$\delta\Pi_e^u = \int_{\Omega_e} \varrho\ddot{\mathbf{u}} \cdot \delta\mathbf{u}\, d\Omega_e + \int_{\Omega_e} \widetilde{\widetilde{\boldsymbol{\sigma}}} : \delta\mathbf{h}\, d\Omega_e - \delta\Pi_e^{u,\text{ext}} + \int_{\Omega_e^n} \left(J_r - \overline{J}_r\right)\delta\overline{p}\, d\Omega_e^n + \int_{\Omega_e^n} \left(\frac{\overline{J}^n}{J^n}\widetilde{p} - \overline{p}\right)\delta\overline{J}_r\, d\Omega_e^n, \tag{37}$$

where $\delta\mathbf{h} = \partial\delta\mathbf{u}/\partial\mathbf{x}$ is the spatial derivative of the virtual displacement field $\delta\mathbf{u}$. The stress quantity $\widetilde{\widetilde{\boldsymbol{\sigma}}}$ and the modified hydrostatic pressure $\widetilde{p}$ are defined as follows

$$\widetilde{\widetilde{\boldsymbol{\sigma}}} = \frac{\overline{J}}{J}\text{dev}\left(\widetilde{\boldsymbol{\sigma}}\right) + \overline{p}\mathbf{I}, \quad \widetilde{p} = \frac{1}{3}\widetilde{\boldsymbol{\sigma}} : \mathbf{I}, \tag{38}$$

where $J = \det(\mathbf{F})$ is the determinant of the deformation gradient at time t_{n+1}, $\overline{J}$ is a scalar related to the volumetric dilatation at time t_{n+1}, and $\widetilde{\boldsymbol{\sigma}}$ is the sum of the modified stresses in branches A and B. It should be noted that the modified stresses in both branches are calculated using the modified total left Cauchy–Green deformation tensor for spring A and the modified deformation tensor for spring B, where $\widetilde{\mathbf{F}}_r$ is used instead of $\mathbf{F}_r$ as follows

$$\widetilde{\mathbf{b}} = \widetilde{\mathbf{F}}_r\widetilde{\mathbf{b}}^n\widetilde{\mathbf{F}}_r^{\text{T}}, \quad \widetilde{\mathbf{b}}_{\text{B}} = \widetilde{\mathbf{F}}_r\left[\mathbf{I} - 2\Delta t\, \widetilde{\mathbf{d}}_{\text{B}}^n\right]\widetilde{\mathbf{b}}_{\text{B}}^n\widetilde{\mathbf{F}}_r^{\text{T}}. \tag{39}$$

In (39), the second order tensor $\widetilde{\mathbf{b}}$ is the modified total left Cauchy–Green deformation tensor and $\widetilde{\mathbf{b}}_{\mathrm{B}}$ is the modified deformation tensor associated with spring B. Also, $\widetilde{\mathbf{d}}_{\mathrm{B}}^{n}$ is the modified deformation rate for the dashpot at time t_n. Assuming that the fields $\bar{J}_r$ and $\bar{p}$ are constants at the element level and vanishing their variations, which are given by the last two terms in the right-hand side of (37), yield the explicit equations for the determination of these fields

$$\bar{J}_r = \frac{1}{\Omega_e^n}\int_{\Omega_e^n} J_r \, d\Omega_e^n, \quad \bar{p} = \frac{1}{\Omega_e^n}\int_{\Omega_e^n} \frac{\bar{J}^n}{J^n}\widetilde{p} \, d\Omega_e^n, \tag{40}$$

where $\bar{J}_r$ as according to (40) can be interpreted as the ratio between the element domain at time t_{n+1} and the element domain at time t_n (i.e., $\bar{J}_r = \frac{\Omega_e}{\Omega_e^n}$), while the field $\bar{p}$ is the average modified hydrostatic pressure within the element domain.

Since the staggered scheme is employed to decouple the displacement and relative mass density fields, the weak form in (35) is linearized with respect to the displacement field as

$$\begin{aligned}\Delta\delta\Pi_e^u = \int_{\Omega_e} \varrho\Delta\ddot{\mathbf{u}}\cdot\delta\mathbf{u}\, d\Omega_e + \int_{\Omega_e}\Bigg\{\delta\mathbf{h} : \left(\widetilde{\mathbb{a}}_{uu} : \Delta\mathbf{h} + \widetilde{\mathbf{a}}_{u\bar{J}_r}\frac{\Delta\bar{J}_r}{\bar{J}_r} + \mathbf{I}\Delta\bar{p}\right) + \frac{\delta\bar{J}_r}{\bar{J}_r}\left(\widetilde{\mathbf{a}}_{\bar{J}_r u} : \Delta\mathbf{h} + \widetilde{a}_{\bar{J}_r\bar{J}_r}\frac{\Delta\bar{J}_r}{\bar{J}_r} - \frac{\bar{J}_r}{J_r}\Delta\bar{p}\right)\\ + \delta\bar{p}\left(\mathbf{I} : \Delta\mathbf{h} - \frac{\bar{J}_r}{J_r}\frac{\Delta\bar{J}_r}{\bar{J}_r}\right)\Bigg\} d\Omega_e,\end{aligned} \tag{41}$$

where the fourth-order tensor $\widetilde{\mathbb{a}}_{uu}$, the second-order tensors $\left\{\widetilde{\mathbf{a}}_{u\bar{J}_r}, \widetilde{\mathbf{a}}_{\bar{J}_r u}\right\}$, and the scalar $\widetilde{a}_{\bar{J}_r\bar{J}_r}$ are, respectively, given by

$$\begin{aligned}\widetilde{\mathbb{a}}_{uu} &= \left(\mathbb{I} - \frac{1}{3}\mathbf{I}\otimes\mathbf{I}\right) : \frac{\bar{J}}{J}\widetilde{\mathbb{a}} : \left(\mathbb{I} - \frac{1}{3}\mathbf{I}\otimes\mathbf{I}\right) - \frac{1}{3}\left(\mathrm{dev}\left(\widetilde{\widetilde{\boldsymbol{\sigma}}}\right)\otimes\mathbf{I} + \mathbf{I}\otimes\mathrm{dev}\left(\widetilde{\widetilde{\boldsymbol{\sigma}}}\right)\right)\\ &\quad + \left(\frac{\bar{J}}{J}\widetilde{p} - \bar{p}\right)\mathbf{I}\oplus\mathbf{I} + \left(\bar{p} - \frac{1}{3}\frac{\bar{J}}{J}\widetilde{p}\right)\mathbf{I}\otimes\mathbf{I},\\ \widetilde{\mathbf{a}}_{u\bar{J}_r} &= \frac{1}{3}\left(\mathbb{I} - \frac{1}{3}\mathbf{I}\otimes\mathbf{I}\right) : \frac{\bar{J}}{J}\widetilde{\mathbb{a}} : \mathbf{I} + \frac{1}{3}\mathrm{dev}\left(\widetilde{\widetilde{\boldsymbol{\sigma}}}\right),\\ \widetilde{\mathbf{a}}_{\bar{J}_r u} &= \frac{1}{3}\mathbf{I} : \frac{\bar{J}}{J}\widetilde{\mathbb{a}} : \left(\mathbb{I} - \frac{1}{3}\mathbf{I}\otimes\mathbf{I}\right) + \frac{1}{3}\mathrm{dev}\left(\widetilde{\widetilde{\boldsymbol{\sigma}}}\right),\\ \widetilde{a}_{\bar{J}_r\bar{J}_r} &= \frac{1}{9}\mathbf{I} : \frac{\bar{J}}{J}\widetilde{\mathbb{a}} : \mathbf{I} - \frac{2}{3}\frac{\bar{J}}{J}\widetilde{p},\end{aligned} \tag{42}$$

where $\mathbb{I}$ is the fourth order unit tensor with components $\mathbb{I}_{ijkl} = \delta_{ik}\delta_{jl}$, and $\widetilde{\mathbb{a}}$ is the modified spatial tangent moduli evaluated according to (A2), where $\left\{\mathbf{F}_r, \mathbf{F}^n\right\}$ are replaced by $\left\{\widetilde{\mathbf{F}}_r, \widetilde{\mathbf{F}}^n\right\}$.

Next, it is advantageous to use the Voigt notation rather than the tensorial notation for finite element derivations. Precisely, in Voigt notation vectors and second-order tensors stored as vectors (indicated by a single underline), whilst fourth-order tensors stored as matrices (indicated by a double underline). In order to approximate the displacement field and the virtual displacement field for each element, the bilinear shape functions for the two-dimensional case and trilinear shape functions for the three-dimensional case are chosen

$$\underline{\mathbf{u}} = \sum_{I=1}^{n_{en}} N_I \underline{\hat{\mathbf{u}}}^I = \underline{\underline{\mathbf{N}}}_u \underline{\hat{\mathbf{u}}}, \qquad \delta\underline{\mathbf{u}} = \sum_{I=1}^{n_{en}} N_I \delta\underline{\hat{\mathbf{u}}}^I = \underline{\underline{\mathbf{N}}}_u \delta\underline{\hat{\mathbf{u}}}, \tag{43}$$

where $\left\{\underline{\hat{\mathbf{u}}}^I, \delta\underline{\hat{\mathbf{u}}}^I\right\}$ denote the displacement vector, and the virtual displacement vector, respectively. Also, n_{en} is the number of nodes per element, and N_I is the shape function for node I. In this section, a three-dimensional formulation for an eight-node brick element is developed for which $n_{en} = 8$. However, the theory is similarly applicable to two-dimensional and axis-symmetric elements, where $n_{en} = 4$. For the finite element development, it is favorable to introduce the following auxiliary vectors

$$\underline{\hat{\mathbf{u}}} = \left\{\underline{\hat{\mathbf{u}}}^1, \underline{\hat{\mathbf{u}}}^2, \ldots, \underline{\hat{\mathbf{u}}}^8\right\}^{\mathrm{T}}, \qquad \delta\underline{\hat{\mathbf{u}}} = \left\{\delta\underline{\hat{\mathbf{u}}}^1, \delta\underline{\hat{\mathbf{u}}}^2, \ldots, \delta\underline{\hat{\mathbf{u}}}^8\right\}^{\mathrm{T}}, \tag{44}$$

which include all nodal displacement vectors, and all nodal virtual displacement vectors, respectively. Likewise, the matrix $\underline{\underline{\mathbf{N}}}_u$ consists of the shape functions N_I. Substituting the approximated displacement field given by $(43)_1$ in the derivative of the variation of the displacement field (i.e., $\delta\mathbf{h} = \partial\delta\mathbf{u}/\partial\mathbf{x}$), the latter can be expressed in terms of the virtual nodal displacements as follows

$$\delta\underline{\mathbf{h}} = \sum_{I=1}^{8} \underline{\underline{\mathbf{B}}}_I \, \delta\underline{\hat{\mathbf{u}}}^I = \underline{\underline{\mathbf{B}}}_u \, \delta\underline{\hat{\mathbf{u}}}, \qquad \underline{\underline{\mathbf{B}}}_u = \left[\underline{\underline{\mathbf{B}}}_1 \quad \underline{\underline{\mathbf{B}}}_2 \quad \dots \quad \underline{\underline{\mathbf{B}}}_8\right], \tag{45}$$

where $\delta\underline{\mathbf{h}} = \{\delta h_{11}, \delta h_{22}, \delta h_{33}, \delta h_{12}, \delta h_{21}, \delta h_{23}, \delta h_{32}, \delta h_{31}, \delta h_{13}\}^{\mathrm{T}}$ is a vector containing the entries of the tensor $\delta\mathbf{h}$, and the matrix $\underline{\underline{\mathbf{B}}}_u$ is the B-matrix for finite deformation, which is of size 9×24 that contains all $\underline{\underline{\mathbf{B}}}_I$, $I = 1, \dots, 8$, while each $\underline{\underline{\mathbf{B}}}_I$ is of size 9×3 that includes the derivatives of the nodes' shape functions with respect to the current coordinates. Now, by substituting $(45)_1$ into (37), the weak form of the linear momentum can be written in terms of nodal forces

$$\delta\Pi_e^u = \delta\underline{\hat{\mathbf{u}}}^{\mathrm{T}} \left(\underline{\hat{\mathbf{F}}}_e^{u,\mathrm{iner}} + \underline{\hat{\mathbf{F}}}_e^{u,\mathrm{int}} - \underline{\hat{\mathbf{F}}}_e^{u,\mathrm{ext}} \right), \tag{46}$$

which include the inertia, internal (due to the constitutive equations), and external (due to external forces) nodal forces

$$\underline{\hat{\mathbf{F}}}_e^{u,\mathrm{iner}} = \int_{\Omega_e} \varrho_0 \gamma \underline{\underline{\mathbf{N}}}_u^{\mathrm{T}} \underline{\ddot{\mathbf{u}}} \, d\Omega_e, \quad \underline{\hat{\mathbf{F}}}_e^{u,\mathrm{int}} = \int_{\Omega_e} \underline{\underline{\mathbf{B}}}_u^{\mathrm{T}} \underline{\tilde{\boldsymbol{\sigma}}} \, d\Omega_e, \quad \underline{\hat{\mathbf{F}}}_e^{u,\mathrm{ext}} = \int_{\partial\Omega_e} \underline{\underline{\mathbf{N}}}_u^{\mathrm{T}} \underline{\bar{\mathbf{t}}} \, d\Gamma_e, \tag{47}$$

where $\underline{\bar{\mathbf{t}}}$ is the external mechanical traction vector, and $\underline{\tilde{\boldsymbol{\sigma}}} = \left\{\tilde{\sigma}_{11}, \tilde{\sigma}_{22}, \tilde{\sigma}_{33}, \tilde{\sigma}_{12}, \tilde{\sigma}_{21}, \tilde{\sigma}_{23}, \tilde{\sigma}_{32}, \tilde{\sigma}_{31}, \tilde{\sigma}_{13}\right\}^{\mathrm{T}}$ is a vector containing the entries of the $\tilde{\boldsymbol{\sigma}}$. The stiffness matrix of the displacement problem can be obtained by substituting (45) into (41)

$$\begin{aligned} \Delta\delta\Pi_e^u = {} & \delta\underline{\hat{\mathbf{u}}}^{\mathrm{T}} \underline{\underline{\mathbf{M}}}_e \, \Delta\underline{\hat{\mathbf{u}}} + \delta\underline{\hat{\mathbf{u}}}^{\mathrm{T}} \left(\underline{\underline{\mathbf{K}}}_e^{uu} \Delta\underline{\hat{\mathbf{u}}} + \underline{\mathbf{K}}_e^{u\bar{J}_r} \frac{\Delta\bar{J}_r}{\bar{J}_r} + \underline{\mathbf{K}}_e^{u\bar{p}} \Delta\bar{p} \right) + \frac{\delta\bar{J}_r}{\bar{J}_r} \left(\underline{\mathbf{K}}_e^{\bar{J}_r u} \Delta\underline{\hat{\mathbf{u}}} + K_e^{\bar{J}_r\bar{J}_r} \frac{\Delta\bar{J}_r}{\bar{J}_r} - K_e^{\bar{J}_r\bar{p}} \Delta\bar{p} \right) \\ & + \delta\bar{p} \left(\underline{\mathbf{K}}_e^{\bar{p}u} \Delta\underline{\hat{\mathbf{u}}} - K_e^{\bar{p}\bar{J}_r} \frac{\Delta\bar{J}_r}{\bar{J}_r} \right). \end{aligned} \tag{48}$$

The mass matrix $\underline{\underline{\mathbf{M}}}_e$ in (48) is defined by

$$\underline{\underline{\mathbf{M}}}_e = \int_{\Omega_e} \varrho_0 \gamma \underline{\underline{\mathbf{N}}}_u^{\mathrm{T}} \underline{\underline{\mathbf{N}}}_u \, d\Omega_e. \tag{49}$$

It can be noticed from (49) that the mass is not conserved within the fractured zone due to crack localization. Thus, contrary to existing methods to model fracture, the MS considers both the loss of stiffness and mass in the fractured zone. Using the static condensation, which allows the elimination of $\Delta\bar{J}_r/\bar{J}_r$ and $\Delta\bar{p}$ and expressing them in terms of $\Delta\underline{\hat{\mathbf{u}}}$, the above linearization can be written as follows

$$\Delta\delta\Pi_e^u = \delta\underline{\hat{\mathbf{u}}}^{\mathrm{T}} \underline{\underline{\mathbf{M}}}_e \, \Delta\underline{\hat{\mathbf{u}}} + \delta\underline{\hat{\mathbf{u}}}^{\mathrm{T}} \underline{\underline{\tilde{\mathbf{K}}}}_e^{uu} \Delta\underline{\hat{\mathbf{u}}}, \tag{50}$$

where the stiffness matrix is defined by

$$\underline{\underline{\tilde{\mathbf{K}}}}_e^{uu} = \underline{\underline{\mathbf{K}}}_e^{uu} + \frac{1}{K_e^{\bar{p}\bar{J}_r}} \underline{\mathbf{K}}_e^{u\bar{J}_r} \underline{\mathbf{K}}_e^{\bar{p}u} + \frac{1}{K_e^{\bar{J}_r\bar{p}}} \underline{\mathbf{K}}_e^{u\bar{p}} \underline{\mathbf{K}}_e^{\bar{J}_r u} + \frac{K_e^{\bar{J}_r\bar{J}_r}}{K_e^{\bar{p}\bar{J}_r} K_e^{\bar{J}_r\bar{p}}} \underline{\mathbf{K}}_e^{u\bar{p}} \underline{\mathbf{K}}_e^{\bar{p}u}. \tag{51}$$

In (51), the matrix $\underline{\underline{\mathbf{K}}}_e^{uu}$, the vectors $\left\{\underline{\mathbf{K}}_e^{u\bar{J}_r}, \underline{\mathbf{K}}_e^{u\bar{p}}, \underline{\mathbf{K}}_e^{\bar{p}u}, \underline{\mathbf{K}}_e^{\bar{J}_r u}\right\}$ and the scalars $\left\{K_e^{\bar{J}_r\bar{J}_r}, K_e^{\bar{J}_r\bar{p}}, K_e^{\bar{p}\bar{J}_r}\right\}$ are given by

$$\begin{aligned} & \underline{\underline{\mathbf{K}}}_e^{uu} = \int_{\Omega_e} \underline{\underline{\mathbf{B}}}_u^{\mathrm{T}} \, \underline{\underline{\tilde{\mathbf{a}}}}_{uu} \, \underline{\underline{\mathbf{B}}}_u \, d\Omega_e, \quad \underline{\mathbf{K}}_e^{u\bar{J}_r} = \int_{\Omega_e} \underline{\underline{\mathbf{B}}}_u^{\mathrm{T}} \, \underline{\tilde{\mathbf{a}}}_{u\bar{J}_r} \, d\Omega_e, \quad \underline{\mathbf{K}}_e^{u\bar{p}} = \int_{\Omega_e} \underline{\underline{\mathbf{B}}}_u^{\mathrm{T}} \, \underline{\mathbf{I}} \, d\Omega_e, \quad \underline{\mathbf{K}}_e^{\bar{p}u} = \int_{\Omega_e} \underline{\mathbf{I}}^{\mathrm{T}} \, \underline{\underline{\mathbf{B}}}_u \, d\Omega_e, \\ & \underline{\mathbf{K}}_e^{\bar{J}_r u} = \int_{\Omega_e} \underline{\tilde{\mathbf{a}}}_{\bar{J}_r u} \, \underline{\underline{\mathbf{B}}}_u \, d\Omega_e, \quad K_e^{\bar{J}_r\bar{J}_r} = \int_{\Omega_e} \tilde{a}_{\bar{J}_r\bar{J}_r} \, d\Omega_e, \quad K_e^{\bar{J}_r\bar{p}} = K_e^{\bar{p}\bar{J}_r} = \int_{\Omega_e} \frac{\bar{J}_r}{J_r} d\Omega_e, \end{aligned} \tag{52}$$

where $\left\{\underline{\underline{\widetilde{\mathbb{a}}}}_{uu}, \underline{\widetilde{\mathbf{a}}}_{u\bar{J}_r}, \underline{\widetilde{\mathbf{a}}}_{\bar{J}_r u}\right\}$ are matrix representation of the tensors $\left\{\widetilde{\mathbb{a}}_{uu}, \widetilde{\mathbf{a}}_{u\bar{J}_r}, \widetilde{\mathbf{a}}_{\bar{J}_r u}\right\}$, respectively. Also, the sizes of $\left\{\underline{\underline{\widetilde{\mathbb{a}}}}_{uu}, \underline{\widetilde{\mathbf{a}}}_{u\bar{J}_r}, \underline{\widetilde{\mathbf{a}}}_{\bar{J}_r u}\right\}$ are $\{9\times 9, 9\times 1, 1\times 9\}$, respectively, and the sizes of $\left\{\underline{\underline{\mathbf{K}}}_e^{uu}, \underline{\mathbf{K}}_e^{u\bar{J}_r}, \underline{\mathbf{K}}_e^{u\bar{p}}, \underline{\mathbf{K}}_e^{\bar{p}u}, \underline{\mathbf{K}}_e^{\bar{J}_r u}\right\}$ are $\{24\times 24, 24\times 1, 24\times 1, 1\times 24, 1\times 24\}$, respectively.

3.2 | Mass balance

The weak form of the mass balance law of typical finite element, is expressed by

$$\delta\Pi_e^{\gamma} = \int_{\Omega_e} \left(-\widetilde{\mathbf{f}}\cdot \operatorname{grad}(\delta\gamma) + \widetilde{\zeta}\,\delta\gamma\right) d\Omega_e, \tag{53}$$

where $\left\{\widetilde{\mathbf{f}},\ \widetilde{\zeta}\right\}$ are the modified $\mathbf{f}$ vector and the modified ζ scalar, which are calculated using $(14)_1$ and (16), respectively, where the modified left Cauchy–Green deformation tensor is used instead of the left Cauchy–Green deformation tensor. The relative mass density field, and the virtual relative mass density field are interpolated inside each element by

$$\gamma = \sum_{I=1}^{n_{en}} N_I \widehat{\gamma}^I = \underline{\mathbf{N}}_{\gamma}\,\underline{\widehat{\gamma}}, \quad \delta\gamma = \sum_{I=1}^{n_{en}} N_I \delta\widehat{\gamma}^I = \underline{\mathbf{N}}_{\gamma}\,\delta\underline{\widehat{\gamma}}, \tag{54}$$

where $\left\{\widehat{\gamma}^I,\ \delta\widehat{\gamma}^I\right\}$ denote the relative mass density scalar, and the virtual relative mass density scalar at node I, respectively. For finite-element development, it is convenient to introduce the following auxiliary vectors

$$\underline{\widehat{\gamma}} = \left\{\widehat{\gamma}^1, \widehat{\gamma}^2, \ldots, \widehat{\gamma}^8\right\}^{\mathrm{T}}, \quad \delta\underline{\widehat{\gamma}} = \left\{\delta\widehat{\gamma}^1, \delta\widehat{\gamma}^2, \ldots, \delta\widehat{\gamma}^8\right\}^{\mathrm{T}}, \tag{55}$$

which include all nodal relative mass density scalars, and all nodal virtual relative mass density scalars, respectively. Also, the row vector $\underline{\mathbf{N}}_{\gamma} = \left\{N_1,\ N_2,\ \ldots, N_{n_{en}}\right\}$ includes the shape functions. The variation of the relative density gradient can be written in terms of the virtual nodal relative mass density by substituting for the virtual relative mass density field from $(54)_2$

$$\operatorname{grad}(\delta\gamma) = \underline{\underline{\mathbf{B}}}_{\gamma}\,\delta\underline{\widehat{\gamma}}, \quad \underline{\underline{\mathbf{B}}}_{\gamma} = \begin{bmatrix} N_{1,1} & N_{2,1} & \ldots & N_{8,1} \\ N_{1,2} & N_{2,2} & \ldots & N_{8,2} \\ N_{1,3} & N_{2,3} & \ldots & N_{8,3} \end{bmatrix}. \tag{56}$$

Now, substituting the developed discretization given in $(54)_2$, and (56) in (53) yields

$$\delta\Pi_e^{\gamma} = \delta\underline{\widehat{\gamma}}^{\mathrm{T}}\,\underline{\widehat{\mathbf{F}}}_{\gamma}^{\mathrm{int}}, \tag{57}$$

where the internal generalized force from the mass balance is articulated as

$$\underline{\widehat{\mathbf{F}}}_e^{\gamma,\mathrm{int}} = \int_{\Omega_e} \left(-\underline{\underline{\mathbf{B}}}_{\gamma}^{\mathrm{T}}\,\widetilde{\mathbf{f}} + \underline{\mathbf{N}}_{\gamma}^{\mathrm{T}}\,\widetilde{\zeta}\right) d\Omega_e. \tag{58}$$

The staggered scheme is used to decouple the displacement and relative mass density fields. Thus, for deriving the stiffness matrix of the mass balance problem, a linearization of (53), with respect to the relative mass density, is required, which is given by

$$\Delta\delta\Pi_e^{\gamma} = -\int_{\Omega_e} \operatorname{Grad}(\delta\gamma)\cdot\widetilde{\mathbf{C}}_{\gamma\gamma}\cdot\operatorname{Grad}(\Delta\gamma)\,d\Omega_e + \int_{\Omega_e} \delta\gamma\,\widetilde{\mathrm{C}}_{\gamma\gamma}\,\Delta\gamma\,d\Omega_e, \tag{59}$$

where the moduli $\widetilde{\mathbf{C}}_{\gamma\gamma}$ and $\widetilde{\mathrm{C}}_{\gamma\gamma}$, respectively, read

$$\widetilde{\mathbf{C}}_{\gamma\gamma} = \frac{\partial\widetilde{\mathbf{f}}}{\partial\left(\operatorname{grad}(\gamma)\right)} = l^2\,\widetilde{\mathbf{b}}, \quad \widetilde{\mathrm{C}}_{\gamma\gamma} = \frac{\partial\widetilde{\zeta}}{\partial\gamma}\Big|_{\left\{J=\bar{J},\ \mathbf{b}=\widetilde{\mathbf{b}}\right\}} = -\frac{\widetilde{I}_3^{1/2}}{\widetilde{\mathcal{H}}+\varepsilon}. \tag{60}$$

Finally, substituting the discretization given in $(54)_2$ and (56) into (59) to develop the relative density tangent stiffness matrix, which is expressed as

$$\underline{\underline{\mathbf{K}}}_e^{\gamma\gamma} = \int_{\Omega_e} \left(-\underline{\underline{\mathbf{B}}}_\gamma^{\mathrm{T}} \, \underline{\underline{\widetilde{\mathbf{C}}}}_{\gamma\gamma} \, \underline{\underline{\mathbf{B}}}_\gamma + \underline{\mathbf{N}}_\gamma^{\mathrm{T}} \, \widetilde{\mathrm{C}}_{\gamma\gamma} \, \underline{\mathbf{N}}_\gamma \right) d\Omega_e. \tag{61}$$

3.3 | Staggered time-integration algorithm

In the event of unstable crack propagation, solving for all degrees of freedom (i.e., displacement and relative density) in one iteration (i.e., fully coupled or monolithic) leads to an unstable solution, that is sometimes can hardly be found.[48] Under those circumstances, the fully coupled scheme is not numerically stable. Thus, in the present study, the staggered (sequentially coupled) method is adopted. It decouples the coupled problem and it alternately solves for the field variables by solving for their respective sub-problems, assuming that the other field variable is constant. Namely, the displacement and the relative density degrees of freedom are solved at the same time independently based on the results obtained from the previous iteration. Thus, on the one hand, the displacement DOFs are obtained by solving the equilibrium equations based on the relative density DOF calculated from the previous iteration. On the other hand, the relative density DOF is obtained by solving the mass balance law based on the displacement DOFs calculated from the previous iteration. Such an alternate minimization technique tremendously boosts the robustness of the obtained solution, allowing to model the crack propagation path (the values of relative density) resulting in each time-step without any convergence issues. Following this approach, the system of equations is written as

$$\begin{bmatrix} \underline{\underline{\widetilde{\mathbf{K}}}}^{uu,\ n+1} & \mathbf{0} \\ \mathbf{0} & \underline{\underline{\widetilde{\mathbf{K}}}}^{\gamma\gamma,\ n+1} \end{bmatrix} \begin{Bmatrix} \Delta\underline{\widehat{\mathbf{u}}}^{n+1} \\ \Delta\underline{\widehat{\gamma}}^{n+1} \end{Bmatrix} = - \begin{Bmatrix} \underline{\widehat{\mathbf{R}}}^{u,\ n+1} \\ \underline{\widehat{\mathbf{R}}}^{\gamma,\ n+1} \end{Bmatrix}, \tag{62}$$

where $\left\{ \underline{\underline{\widetilde{\mathbf{K}}}}^{uu,\,n+1}, \underline{\underline{\widetilde{\mathbf{K}}}}^{\gamma\gamma,\,n+1} \right\}$ are the assembled stiffness matrices, $\left\{ \underline{\widehat{\mathbf{R}}}^{u,\,n+1}, \underline{\widehat{\mathbf{R}}}^{\gamma,\,n+1} \right\}$ are the assembled residuals of displacement $\Delta\underline{\widehat{\mathbf{u}}}^{n+1}$ and relative density $\Delta\underline{\widehat{\gamma}}^{n+1}$ sub-problems, respectively, at the end of the current increment.

To analyze the dynamic response of the material, a time integration method should be employed. There is a number of options regarding which time integration operator should be adopted to solve the problem at hand. For example, Newmark-beta method,[49] Wilson θ-method,[50,51] generalized-α scheme,[52] Hilber–Hughes–Taylor (HHT) method,[53] or Park method[54] can be chosen. Such a choice is based on different criteria. For instance, unconditional or conditional stability of the proposed method, its second order accuracy, and if it is computationally efficient. In particular, Abaqus uses the HHT integrator[53] for dynamic cases, which is an implicit method allowing for second order accuracy, which is not achievable using the regular Newmark method. The HHT operator is characterized by a controllable numerical damping, and it replaces the original equilibrium equation with a balance of d'Alembert forces at the end of the time increment and a weighted average of the forces at the beginning and end of the time increment.[38] Specifically, the HHT scheme solves the linearized equilibrium equations in (62) by applying a Newton-Raphson iteration, in which the displacement residual is defined as

$$\underline{\widehat{\mathbf{R}}}^{u,\ n+1} = \mathop{\mathbf{A}}_{e=1}^{N_{el}} \left[\underline{\widehat{\mathbf{F}}}_e^{\mathrm{iner},\ n+1} + (1+\alpha) \left(\underline{\widehat{\mathbf{F}}}_e^{u,\mathrm{int},\ n+1} - \underline{\widehat{\mathbf{F}}}_e^{u,\mathrm{ext},\ n+1} \right) - \alpha \left(\underline{\widehat{\mathbf{F}}}_e^{u,\mathrm{int},\ n} - \underline{\widehat{\mathbf{F}}}_e^{u,\mathrm{ext},\ n} \right) \right], \tag{63}$$

where the displacement residual contains internal (int), external (ext), and inertial (iner) components, and the parameter α is a damping coefficient. Likewise, the relative density residual is defined as follows

$$\underline{\widehat{\mathbf{R}}}^{\gamma,\ n+1} = \mathop{\mathbf{A}}_{e=1}^{N_{el}} \left[(1+\alpha) \underline{\widehat{\mathbf{F}}}_e^{\gamma,\mathrm{int},\ n+1} - \alpha \underline{\widehat{\mathbf{F}}}_e^{\gamma,\mathrm{int},\ n} \right]. \tag{64}$$

The stiffness matrices of the displacement and relative density sub-problems, respectively, are defined as

$$\underline{\underline{\widetilde{\mathbf{K}}}}^{uu,\ n+1} = \mathop{\mathbf{A}}_{e=1}^{N_{el}} \left[\frac{1}{\mu\Delta t^2} \underline{\underline{\mathbf{M}}}_e^{n+1} + (1+\alpha) \underline{\underline{\widetilde{\mathbf{K}}}}_e^{uu,\ n+1} \right], \quad \underline{\underline{\widetilde{\mathbf{K}}}}^{\gamma\gamma,\ n+1} = \mathop{\mathbf{A}}_{e=1}^{N_{el}} (1+\alpha) \underline{\underline{\mathbf{K}}}_e^{\gamma\gamma,\ n+1}, \tag{65}$$

TABLE 1 Abdominal aortic aneurysm material parameters.

Φ_A (MPa)	m	k^{A}_{bulk} (MPa)	k^{B}_{bulk} (MPa)	c^{A}_{1} (MPa)	c^{B}_{1} (MPa)	c^{A}_{2} (MPa)	c^{B}_{2} (MPa)	l (mm)	ρ_0 (kg/m^3)
0.1686	10	500	500	0.617	0.617	1.215	1.215	0.1	1433

in which the stiffness matrix of the displacement sub-problem includes the mass matrix $\underline{\underline{\mathbf{M}}}_e$ defined as in (49), with $\mu = (1-\alpha)^2/4$.

4 | NUMERICAL EXPERIMENTS

In this section, we investigate the numerical performance of the nonlinear viscoelastic MS fracture model. The two-dimensional domains are discretized with four-node quadrilateral elements assuming plane strain conditions. On the other hand, three-dimensional domains are discretized with eight-node brick elements. All meshes used in this study are unstructured meshes, where the elements have random patterns. The specific form of the strain energy functions for springs A and B are, respectively, given by

$$W = \underbrace{\frac{1}{2}k^{A}_{bulk}(J-1)^2 + c^{A}_{1}(\eta-3) + c^{A}_{2}(\eta-3)^2}_{W_A(\mathbf{b})=W_A(J,\eta)} + \underbrace{\frac{1}{2}k^{B}_{bulk}(J_B-1)^2 + c^{B}_{1}(\eta_B-3) + c^{B}_{2}(\eta_B-3)^2}_{W_B(\mathbf{b}_B)=W_B(J_B,\eta_B)}, \tag{66}$$

where the invariants $J = \det(\mathbf{F})$ and $\eta = J^{-2/3}\mathbf{b} : \mathbf{I}$ control the volumetric deformation and the distortional deformation, respectively. Also, the invariants $J_B = \sqrt{\det(\mathbf{b}_B)}$ and $\eta_B = J_B^{-2/3}\mathbf{b}_B : \mathbf{I}$ control, respectively, the elastic volumetric deformation and the elastic distortional deformation associated with spring B. The strain energy functions of spring A and B depend on the material parameters k^{A}_{bulk}, c^{A}_{1}, c^{A}_{2} and k^{B}_{bulk}, c^{B}_{1}, c^{B}_{2}, respectively.

The material under consideration is a sample from an abdominal aortic aneurysm (AAA) with material parameters tabulated in Table 1, and the adopted parameters for the HHT integrator are $\{\alpha = -0.05, \mu = 0.275625\}$.

4.1 | Relaxation and creep tests

A three-dimensional cube—with 1 mm long faces—is modeled under uniaxial tension (i.e., patch test). The MS (damage) is not active in this example. That is to say, the material behaves viscoelastically without fracture. The main objective of this example is to test the viscoelastic response without any material degradation and to investigate the effect of the viscosity parameter β_2 on the relaxation and creep responses of the material.

In the relaxation test, the simulation is carried out in two steps. In the first step, the cube is under a uniaxial displacement increasing from 0.0 mm to 1.0 mm corresponding to times 0.0 and 0.0001 s, respectively. In the second step, the displacement is kept at 1 mm till the end of the simulation. Figure 2A depicts the resulting relaxation force versus time for different values of the viscosity parameter β_2. The results show that the relaxation graphs are bounded by two limits. The bottom bound is when spring A alone is active. On the other hand, the top bound is when both springs A and B are active while the dashpot is deactivated. Increasing the viscosity parameter increases the relaxation time as shown in Figure 2A. Moreover, the relaxation curves are close to each other under the increase of the viscosity parameter. The latter implies that the material response is more sensitive to the change of the viscosity parameter when the viscosity is small.

In the creep test, in the first step, a load is applied varying from 0.0 to 10.0 N, corresponding to times 0.0 and 0.001 s, respectively. In the second step, the load is maintained to 10.0 N until the end of the simulation. Figure 2B shows the resulting displacement versus time for different values of the viscosity parameter. It can be noticed that there are two—lower and upper—bounds limiting the minimum and maximum displacements. The upper bound is when spring A works partnerless. However, the lower bound corresponds to the case when both springs work without the dashpot. The viscosity parameter plays its role between those two limits; as the viscosity parameter increases, the creep time increases. Increasing the viscosity parameter at a constant pace, it can be noticed that the distance between curves narrows down,

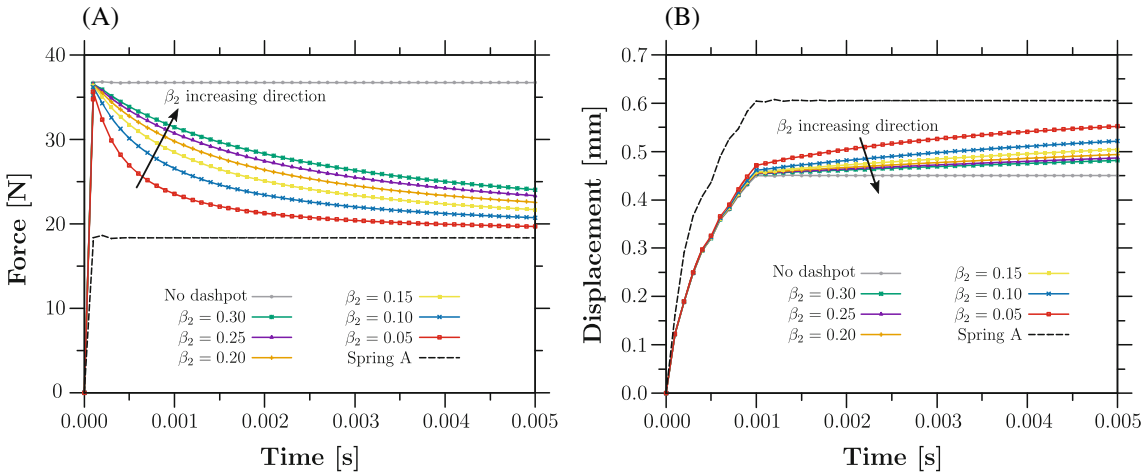

FIGURE 2 Relaxation and creep tests under the change of the viscosity parameter β_2: (A) Force versus time from the relaxation test, (B) displacement versus time from the creep test. The viscosity parameter β_2 has units of MPa s.

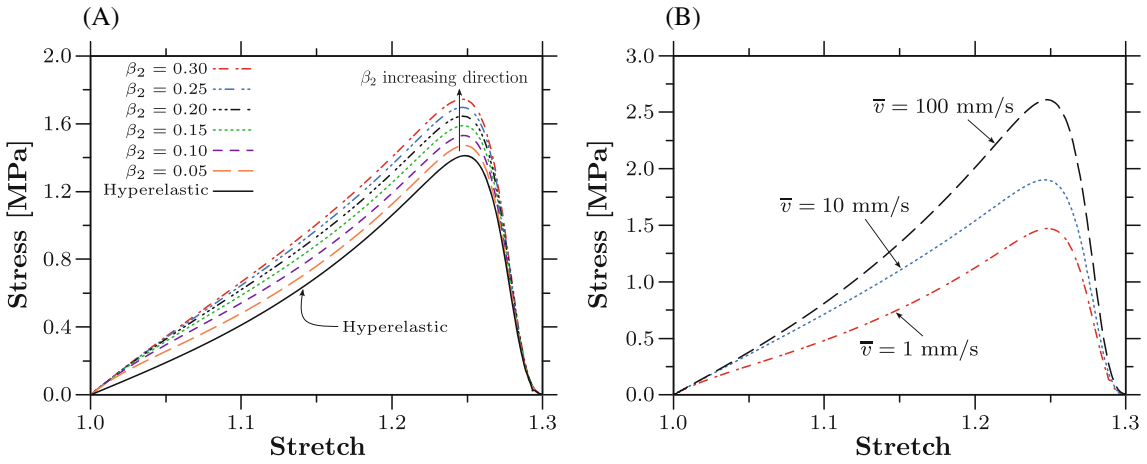

FIGURE 3 Stress-stretch curves for AAA material from uniaxial tension test: (A) The viscosity parameter is variable while the applied velocity is constant, (B) the applied velocity is variable while the viscosity parameter is constant. The viscosity parameter β_2 has units of MPa s.

implying that sensitivity to the viscosity parameter increases as the viscosity decreases. Clearly, the proposed viscoelastic model captures the relaxation and creep behaviors of the material.

4.2 | Uniaxial tension test

A cube with edges that have a 1 mm length is modeled in this example. The MS (fracture) is active in this example and in all subsequent examples. The specimen is created from AAA material with parameters summarized in Table 1. Figure 3A shows the stress-stretch curves for different values of the viscosity parameter β_2. The applying velocity is kept constant for all cases, having a value of 1 mm/s. In Figure 3A, the solid line is for the hyperelastic case, where the result matches the result documented by Faye et al.[36] On the other hand, the dashed and dotted lines are for the viscoelastic cases. It can be noticed that increasing the viscosity shifts the curve upward.

Figure 3B depicts the stress-stretch curves for different values of the applied velocity. A constant viscosity parameter equals 0.05 MPa s is used in this comparison. Three values of the applied velocity are used, equaling 1, 10, and 100 mm/s. It can be noticed from Figure 3B that when the load is applied fast the material bears more stress, which manifests the effect of the viscosity.

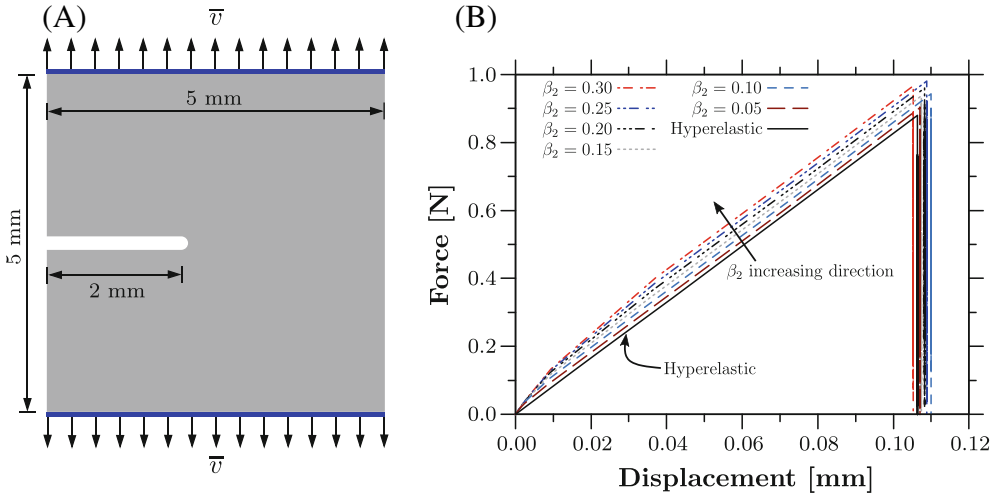

FIGURE 4 Single-edge notched sample under uniaxial tension: (a) Geometry and boundary conditions and (B) reaction force versus displacement curves grouped by the change of the viscosity parameter β_2. The viscosity parameter β_2 has units of MPa s.

4.3 | Single-edge notched sample under uniaxial tension

In this subsection, we investigate the effects of the viscosity on the fracture pattern of a sample under uniaxial tension. The sample is a square sample created from an abdominal aortic aneurysm with parameters tabulated in Table 1, comprising a preexisting notch. The top and bottom edges are under a velocity of 0.1 mm/s applying in the vertical direction as depicted in Figure 4A.

Figure 4B illustrates the force versus displacement responses for the hyperelastic and viscoelastic cases. For the viscoelastic case, different values of the viscosity parameter β_2 are used and the force versus displacement curve for each case is plotted. It can be noticed from Figure 4B that the solid bottom line represents the hyperelastic case and the dashed lines represent the viscoelastic cases. Evidently, increasing the value of the viscosity parameter shifts the graph upward because of the over-stress contribution induced by the viscosity.

The first row in Figure 5 shows the relative density (γ) contours for the hyperelastic and viscoelastic cases. The relative density values range between 0 and 1, where a value of 1 means that the material is intact and a value of 0 means that the material is totally fractured. It can be noticed from the first row in Figure 5 that the crack pattern for the viscoelastic cases is different than the hyperelastic one. The crack pattern is less branching in the viscoelastic cases due to the viscosity dissipative mechanisms taking account during crack propagation.

The numerical experiments are re-conducted, adopting a higher applied velocity having a value of 100 mm/s. The resulting relative density contours (damage) are shown in the second row in Figure 5, where it can be noticed that the viscosity does not affect the crack propagation path. In other words, at high strain rates, the material behaves hyperelastically, undermining the viscosity effect. It can be concluded that the viscosity affects the crack propagation path only at small strain rates.

4.4 | Sample with an inclined notch under uniaxial tension

A squared sample with an inclined notch is tested in this example. The notch has a length of 1 mm and is inclined at an angle of 45°. A velocity of 0.1 mm/s is applied on the top and bottom edges in the vertical direction as depicted in Figure 6A. The sample is created from an abdominal aortic aneurysm material with properties summarized in Table 1.

The simulations are conducted on two cases. The first case is when the material behaves hyperelastically, and the second case is when the material behaves viscoelastically with a viscosity parameter β_2 equals 0.05 MPa s. Figure 6B,C show the deformed shapes for both cases, respectively.

For both cases, a crack initiates from each side of the preexisting notch propagating in a straight line perpendicular to the tensile loading direction following the mode I direction until reaching the end of the sample. However, in the

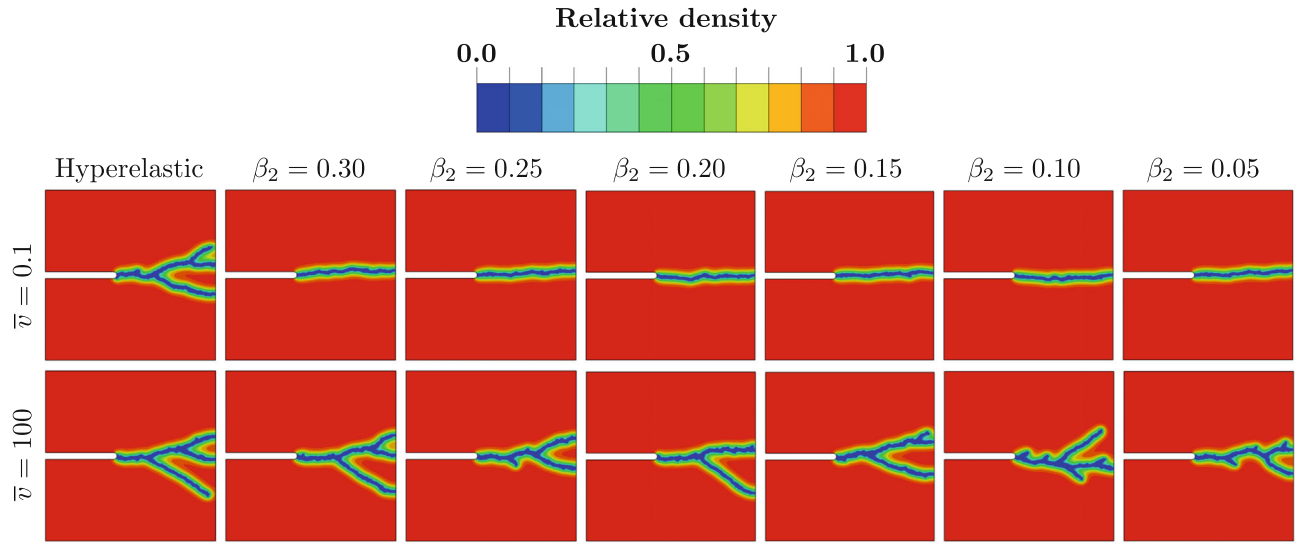

FIGURE 5 Relative density (i.e., γ) contours for the single-edge notched sample under uniaxial tension for the hyperelastic case and the viscoelastic cases grouped by the change of the viscosity parameter β_2. The first and second rows designate the cases when the applied velocities equal 0.1 and 100 mm/s, respectively. The viscosity parameter β_2 has units of MPa s.

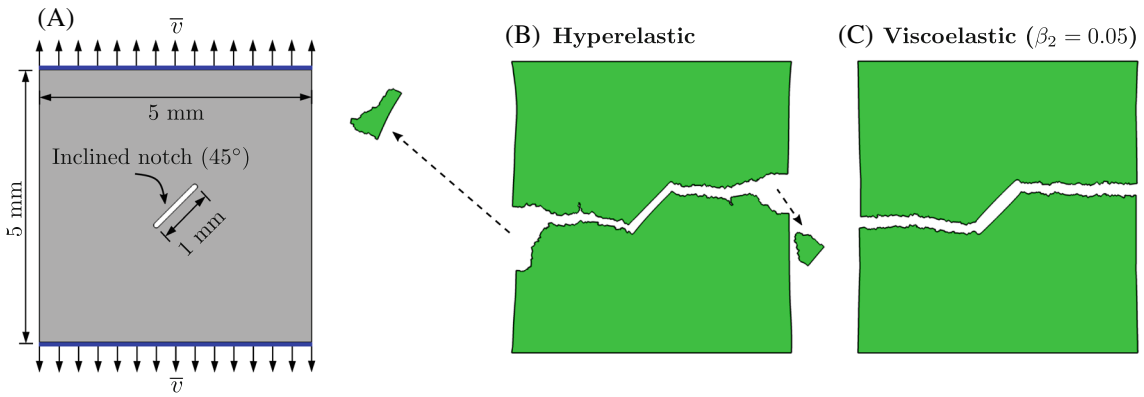

FIGURE 6 Sample with an inclined notch under uniaxial tension: (A) Geometry and boundary conditions, (B) and (C) deformed configurations for the hyperelastic and viscoelastic cases, respectively. The viscosity parameter β_2 has units of MPa s.

hyperelastic case, the crack incorporates branches that do not exist in the viscoelastic case. The crack pattern in the viscoelastic case is much smoother and has less tendency to branch compared to the hyperelastic case. Figure 8A shows the force versus displacement curves for the hyperelastic and viscoelastic cases, where the viscoelastic graph is shifted upward compared to the hyperelastic case.

Figure 7 shows the crack paths for different samples. The samples have notches inclined with different angles as shown in the top row of Figure 7. The samples are viscoelastic with viscosity parameter β_2 equals 0.05 MPa s, where they have the same boundary conditions and dimensions as shown in Figure 6A. The samples fracture in straight paths as shown in Figure 7, where no branching was noticed. Figure 8B shows the force versus displacement curves for all the different angles cases. It can be noticed that when the inclination angle increases, the force and displacement at which the material develops cracks increase as well. The latter is justifiable, since when the notch is completely perpendicular to the loading direction (i.e., $\theta = 0°$), the material has the less resistance to crack propagation, which will increase by increasing the inclination angle. It can be noticed from Figure 8B that for $\theta = 30°$, the sample fractures in two steps. The latter because the crack initiates and propagates first from the left side of the notch until reaching the end of the sample. Afterwards, another crack initiates and propagates from the right side of the notch, fracturing the specimen in two steps. It is interesting to note the slight increase in stiffness for $\theta = 75°$ after a certain displacement. The latter occurs because

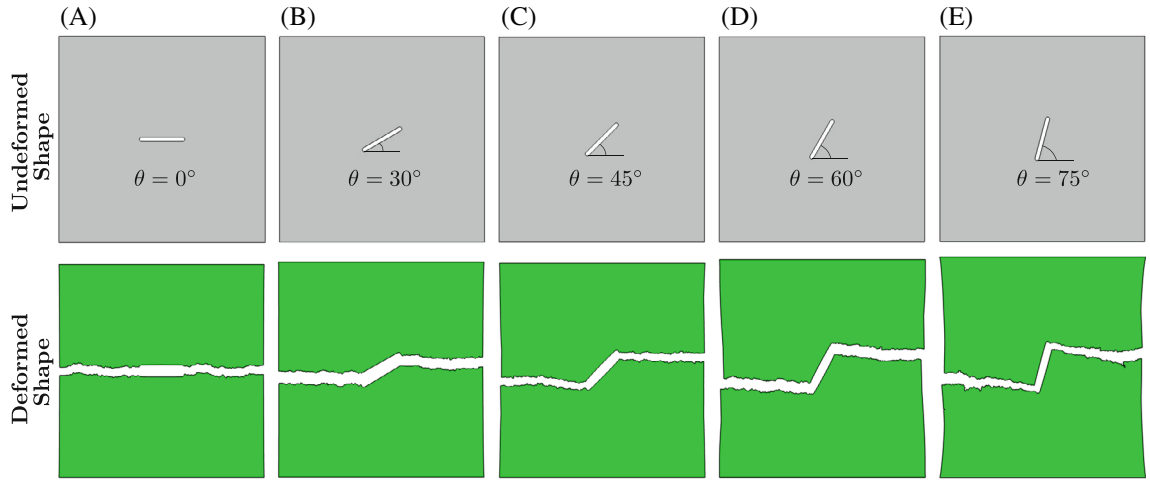

FIGURE 7 Samples having notches inclined with different angles under uniaxial tension for the viscoelastic cases: (A) $\theta = 0°$, (B) $\theta = 30°$, (C) $\theta = 45°$, (D) $\theta = 60°$, (E) $\theta = 75°$. The top and bottom rows are for the undeformed and deformed shapes, respectively.

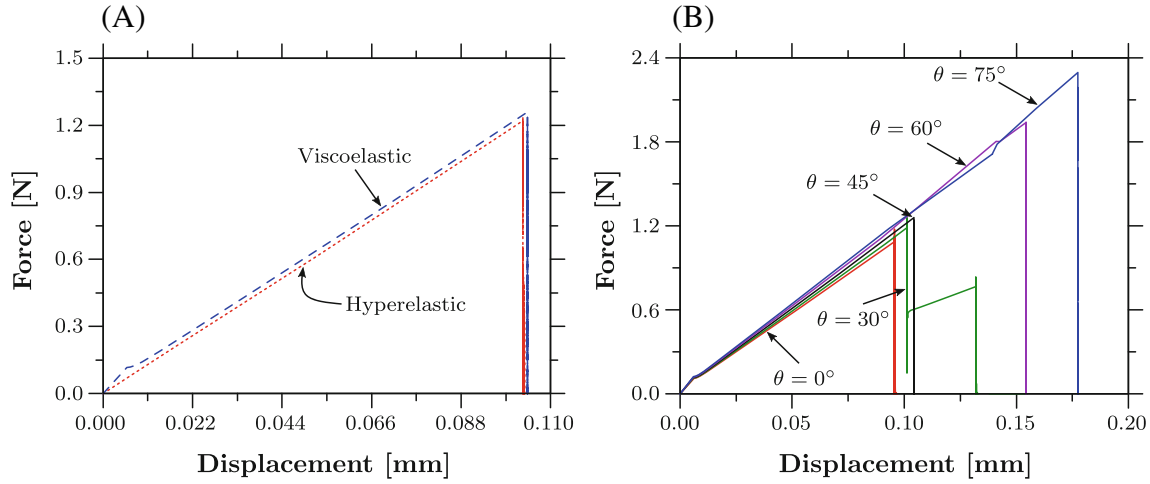

FIGURE 8 Force versus displacement curves for the inclined notch sample: (A) For the hyperelastic and viscoelastic cases when $\theta = 45°$, and (B) for the viscoelastic cases for different values of θ.

when the inclination angle is large, the stress is concentrated at four corners as well as on both sides of the notch just before crack initiation. Then the cracks propagate from both sides of the notch, relieving the corners of the sample, which increases its stiffness.

4.5 | Strip sample

A rectangular strip of 6 mm length and 3 mm width is tested for tensile loading, created from AAA material with material parameters tabulated in Table 1. The sample has two holes of diameter 1 mm arranged on right and left alternately. A prescribed tensile velocity is applied on the right and left ends having a value of 1 mm/s as depicted in Figure 9A. No initial crack is introduced, the relative density variable begins to evolve at the place of strain energy concentrations. The unstructured mesh is refined in the regions where the crack is expected to propagate, that is, in the middle two-third of the specimen.

The simulations are carried out on both hyperelastic and viscoelastic ($\beta_2 = 0.05$ MPa s) materials and the resulting deformed configurations are shown in Figure 9B,C, respectively. In the hyperelastic case, a crack starts to initiate and

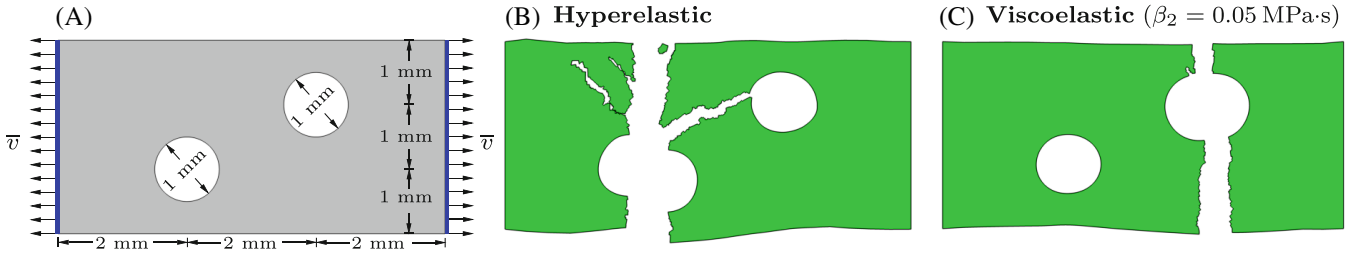

FIGURE 9 Strip under tension: (A) Geometry and boundary conditions, (B) and (C) deformed configurations for the hyperelastic and viscoelastic cases, respectively.

propagates from the bottom side of the left hole until reaching the bottom side of the specimen. Thereafter, a crack initiates from the top side of the same hole propagating in the upward direction until the full fracture of the sample. In the viscoelastic case, a crack starts to initiate and propagates from the bottom side of the right hole until reaching the bottom side of the specimen. Thereafter, a crack initiates from the top side of the same hole propagating in the upward direction until the full fracture of the sample.

It is noted from Figure 9 that the fracture pattern propagating in the hyperelastic medium incorporates more branching compared to the crack propagating in the viscoelastic medium. In other words, the viscosity regularizes the propagating crack by curbing its willingness to branch. All the examples in this study demonstrate that the viscosity affects the crack propagation path when the applied strain rate is small, leading to fracture patterns with less branching compared to the hyperelastic case. It is noteworthy to notice the debris flying during crack propagation in Figure 9, it is clear that considering the loss of inertia as a result of losing material, is the most realistic scenario occurring as a result of specimen's separation. In other words, the MS method considers the loss of material not only as lost stiffness but as lost mass as well.

4.6 | Three-dimensional dog-bone shaped sample

Modeling cracks in 3D samples is not different than modeling cracks in 2D samples using the MS method. In other words, the MS approach models cracks in 3D solids without the need to generalize the theory for the additional dimension. In this subsection, a 3D dog-bone-shaped sample created from AAA material is simulated for crack propagation, where the material behaves viscoelastically with viscosity parameter $\beta_2 = 0.05$ MPa s.

The specimen is under a uniaxial tension applied in the vertical direction as shown in Figure 10A. A prescribed velocity of 1 mm/s is applied in the positive y-direction on the top surface and a velocity of 1 mm/s is applied in the negative y-direction on the bottom surface, while the top and bottom surfaces are restricted to moving in the x and z-directions. The sample has a thickness of 0.2 mm, and it is discretized with 20,955 eight-node brick elements, with one element throughout the thickness.

In order to reach higher values of stretches until fracture, a modified AAA material is utilized. Two cases are modeled where the energy limiter Φ for the modified AAA material has been elevated to 1 MPa and 5 MPa, respectively. Figure 11A shows the stress versus stretch curves for both cases of the modified AAA material from the patch test. When $\Phi = 1$ MPa, the stretch at which the material fractures is 1.58, and when $\Phi = 5$ MPa, the stretch at which the material fractures is 2.03. Figure 11B shows the force versus displacement curves resulted from modeling the dog-bone shaped sample for both cases, when $\Phi = 1$ MPa and $\Phi = 5$ MPa, accordingly. It is clear that the relation between the value of the energy limiter and the critical stretch at which the material fails is not linear.

The resulting fracture patterns are shown in Figure 10B,C for $\Phi = 1$ and $\Phi = 5$, respectively. In both cases, cracks propagate at the intersection points between the fillets and the narrow sections that merge with their counterparts coming from the other side until complete fracture of the sample into three pieces. In this example, there is no a preexisting crack or a notch introduced in the sample's domain. The cracks initiated at the places of stress concentration induced by the merging between the curve of the fillet with the stem. The simulations also demonstrate the easiness of modeling cracks in 3D domains using the MS method.

Furthermore, the implicit scheme discussed in Section 2.3 has been employed in this example for the case when $\Phi = 5$ MPa. Figure 12 shows the force versus displacement curves from the explicit and implicit schemes. It can be noticed that there is no difference in the results from both schemes before crack propagation, yet there is a slight difference when the crack propagates, where the difference is marginal.

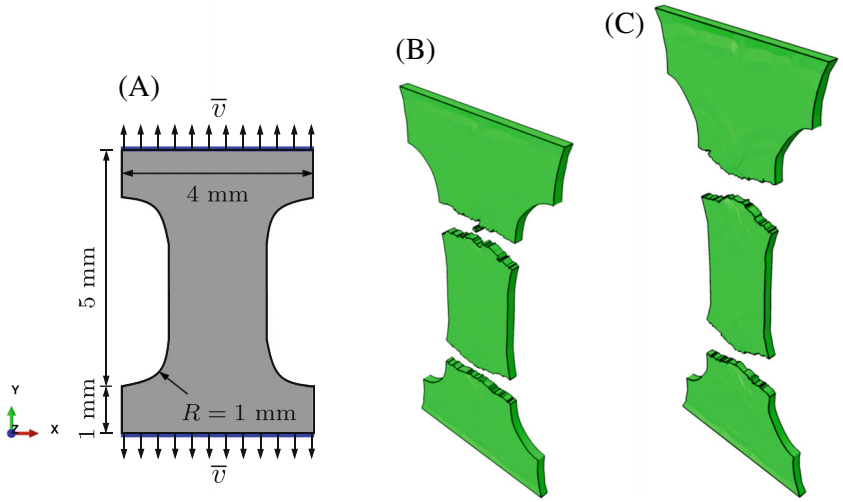

FIGURE 10 3D dog-bone sample under tension: (A) Geometry and boundary conditions, (B) and (C) deformed configurations for $\Phi = 1$ MPa and $\Phi = 5$ MPa, respectively.

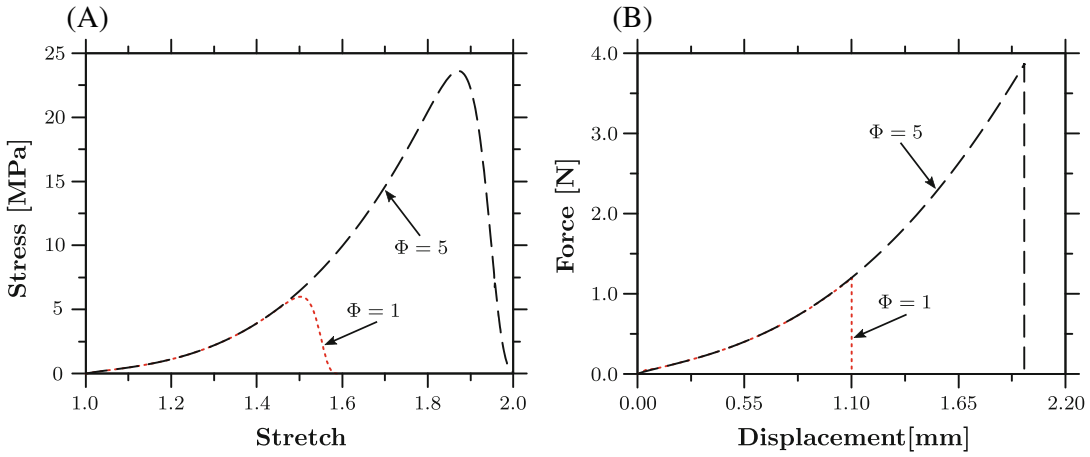

FIGURE 11 Modified AAA material: (A) Stress versus stretch curves from patch test, (B) force versus displacement curves from the 3D dog-bone sample under tension for $\Phi = 1$ MPa and $\Phi = 5$ MPa.

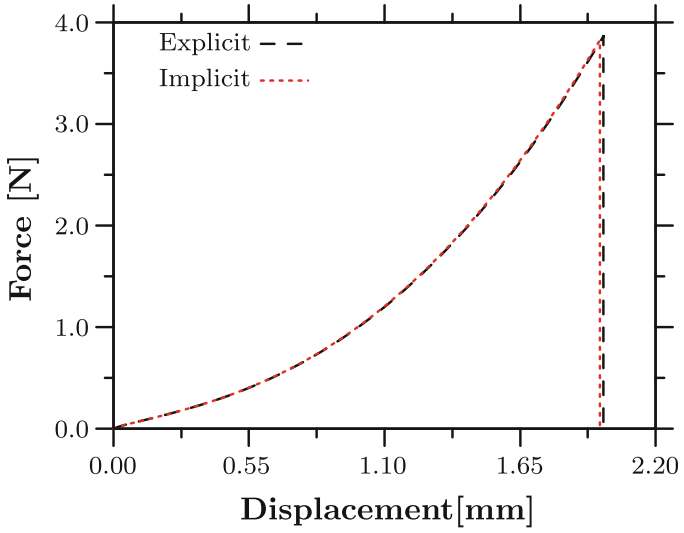

FIGURE 12 Force versus displacement curves from the 3D dog-bone sample under tension for $\Phi = 5$ MPa using both the explicit and implicit schemes.

4.7 | Tearing test

An out-plane tearing test (mode III fracture) is simulated, where the geometric setup is shown in Figure 13A, with in-plane (i.e., x–y plane) dimensions the same as in Figure 4A and a thickness of 0.2 mm, and it is discretized with 24,800 eight-node brick elements, with four elements throughout the thickness. The left side is restrained, and an out-plane tear is applied on the edge of the right part with an applied velocity equals 1 mm/s in the z-direction. The material under consideration is the standard AAA material with parameters tabulated in Table 1 and a viscosity parameter β_2 equals 0.1 MPa s.

The crack propagation progression is shown in Figure 13B–E, in which a crack initiates from the preexisting notch and propagates in a path parallel to the x-direction until the final fracture. The result shows good agreement with results obtained by Yin and Kaliske.[55] Figure 14 shows the force versus displacement curve, where the crack evolution for each fracture stage is shown on the same figure. The force keeps increasing smoothly until reaching a critical limit, then the material starts failing and the crack starts initiating within the sample's domain. After this point, the force fluctuates during crack propagation due to the resistance of the sample to damage. Finally, the force reaches zero and the sample is completely fractured into two pieces.

4.8 | Peeling test

A peeling test is modeled, in which the geometric setup of a three-dimensional sample with a preexisting notch is shown in Figure 15A having a thickness of 0.2 mm. An applied velocity of 1 mm/s is applied on the left side in the positive and negative vertical directions as shown in Figure 15A, where the specimen is restricted to moving in the z-direction (thickness direction) and fixed at the right edge. The material under consideration is the standard AAA material with parameters tabulated in Table 1 and a viscosity parameter β_2 equals 0.05 MPa s. The crack diverges towards the bottom until it fractures the specimen into two pieces, as shown in Figure 15B–D. At first glance, the reader might think that the crack should propagate in a fairly straight line, cutting the sample into two equal pieces. However, this is not the case! Because in reality, if the load is applied solely on the left part—it is not distributed on the entire top and bottom sides—the crack will diverge as a result of the load (that is normal to the plane of the preexisting crack) being not continuous and rather concentrated only at the beginning of the preexisting crack. In Reference 55, the peeling test lead to a crack propagating in a straight line through the sample. The latter occurred because the authors in Reference 55 analyzed only half of the sample due to symmetry. However, evidently, it is not totally accurate to only model half of the sample—even when symmetry is present—in such fracture problems. Since using only half of the sample, the real problem would not be well represented, whereupon an unrealistic crack path will be acquired. The same peeling test is re-conducted while allowing the specimen to move in the z-direction, where the resulting fracture pattern is shown in Figure 16A–D. The crack starts propagating in a straight path and then kinks up towards the top of the specimen until full fracture.

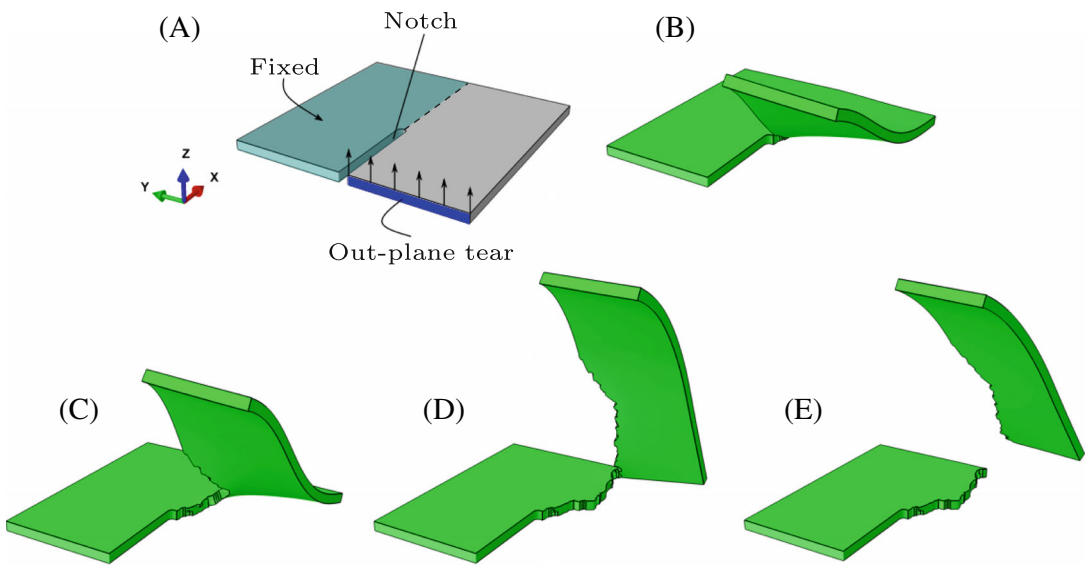

FIGURE 13 Tearing test of a three-dimensional sample: (A) Geometry and boundary conditions, (B–E) fracture evolution.

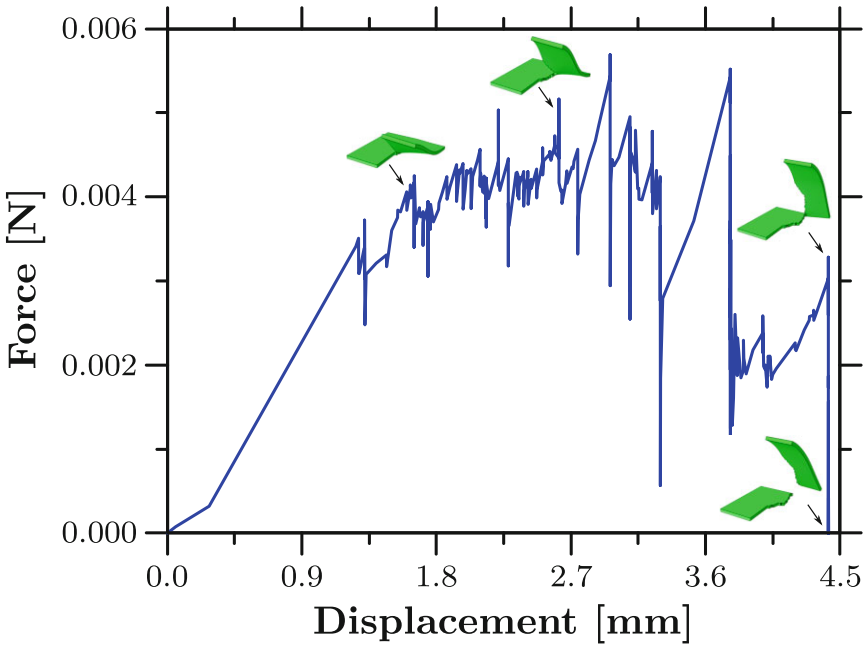

FIGURE 14 Force versus displacement curve (in the z-direction) from the tearing test of a three-dimensional sample. Crack evolution for each fracture stage is shown on the same figure. For a larger image of the crack evolution, the reader might refer to Figure 13B–E.

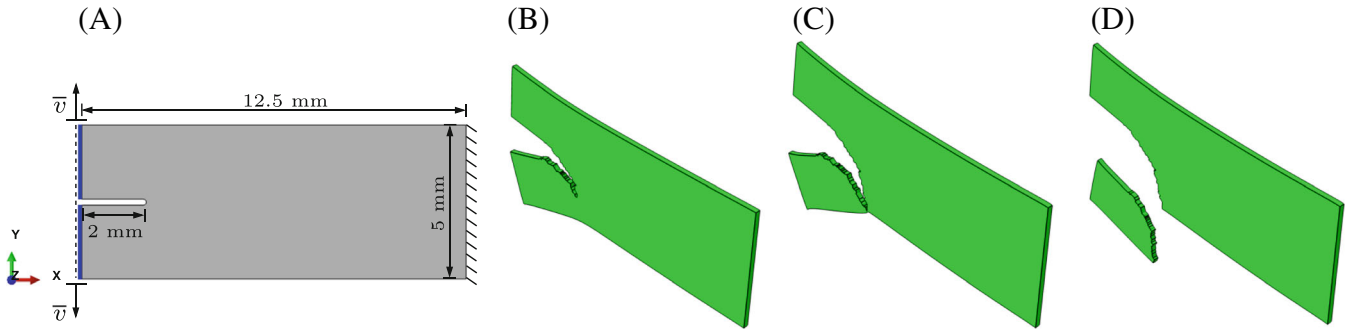

FIGURE 15 Peeling test of a three-dimensional specimen restrained to moving in the z-direction: (A) Geometry and boundary conditions, (B)–(D) fracture evolution.

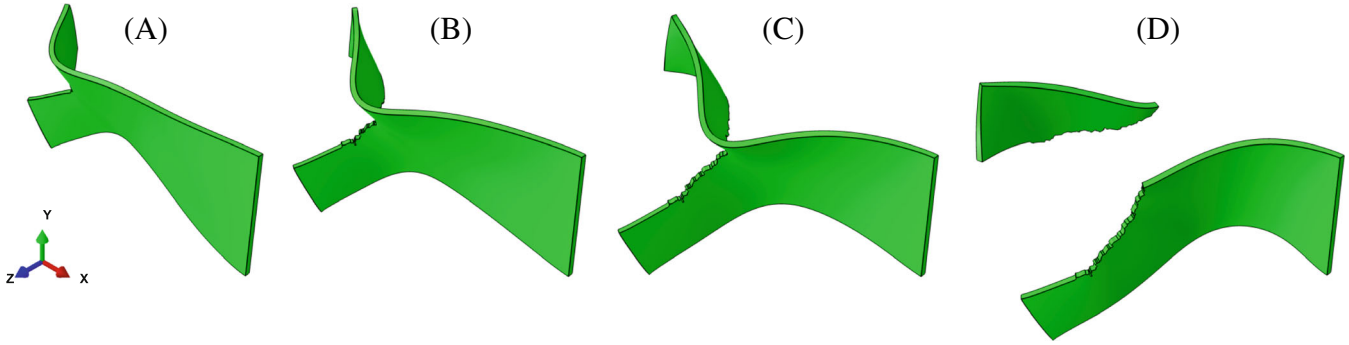

FIGURE 16 Fracture evolution in a peeling test of a three-dimensional specimen not restricted to moving in the z-direction.

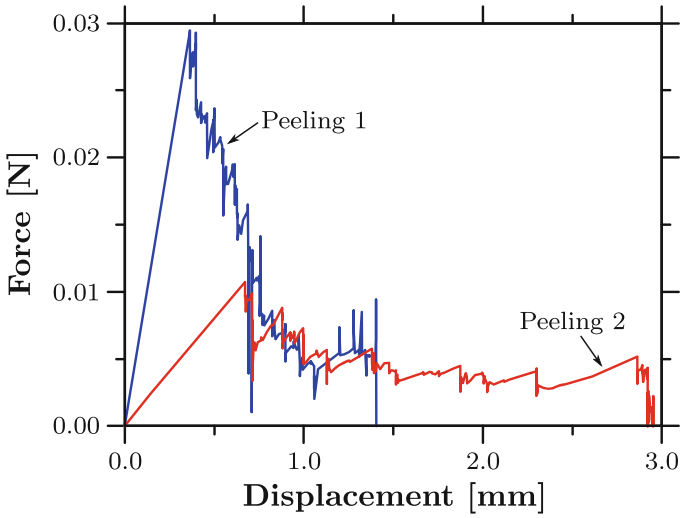

FIGURE 17 Force versus displacement curves (in the y-direction) from peeling tests. Peeling 1 designates the case when the specimen is restrained to moving in the z-direction, and Peeling 2 designates the case when the specimen is unrestrained to moving in the z-direction.

Figure 17 shows the force versus displacement curves for the peeling tests. Peeling 1 curve designates the case when the specimen is restrained to moving in the z-direction, and Peeling 2 curve designates the case when the specimen is unrestrained to moving in the z-direction. The forces increase until reaching an ultimate point, after which the forces decrease with fluctuation due to crack propagation. It can be noticed that the maximum force at which the material develops cracks is higher for Peeling 1 compared to Peeling 2. On the other hand, the displacement at which the sample is completely separated is higher for Peeling 2 compared to Peeling 1.

5 | CONCLUSIONS

A nonlinear viscoelasticity theory was coupled with the MS method. The proposed method was used to model fracture in viscoelastic materials under large deformation. In order to overcome the locking behavior resulting from modeling incompressible materials using the standard FEM, a mixed finite element approach based on the relative deformation gradient has been adopted. The proposed approach was implemented in the commercial software Abaqus using the user-defined element subroutine (UEL) via a three-layers concept.

It has been shown that the proposed method captures the relaxation and creep behaviors of the material. Further, through different 2D and 3D examples, it has been demonstrated that the crack propagation path in hyperelastic materials is different from the crack propagation path in viscoelastic materials when the applied strain rate is relatively small. The fracture pattern in viscoelastic materials has less tendency to branch compared to the fracture pattern in hyperelastic materials. In other words, viscosity plays a regularization effect during the crack propagation process by reducing the crack's willingness to branch. However, when the applied strain rate is relatively high, the crack propagating in viscoelastic and hyperelastic materials incorporates branching.

ACKNOWLEDGMENTS

The support from the Israel Science Foundation (ISF-394/20) as well as the Israeli Ministry of Science and Technology (MOST-0005173) is gratefully acknowledged. Also, M. Jabareen is supported by Neubauer Foundation.

DATA AVAILABILITY STATEMENT

The data that support the findings of this study are available from the corresponding author upon reasonable request.

ENDNOTES

*Failure refers to the onset of damage as material instability, whereas fracture refers to the damage localization into cracks.[4]

†Maxwell model is an arrangement of spring and dashpot connected in series that is named after J. C. Maxwell.

‡Branch A corresponds to the thermodynamic equilibrium states of the material, while branch B corresponds to the non-equilibrium states or over-stress contribution.
§Layer in this context means a finite-element. So, when we use three layers, it means three finite-elements overlay each other, sharing the same nodes and integration points.

ORCID

Suhib Abu-Qbeitah https://orcid.org/0000-0002-9318-6910
Mahmood Jabareen https://orcid.org/0000-0002-0442-9053
Konstantin Y. Volokh https://orcid.org/0000-0002-2770-3916

REFERENCES

1. Abu-Qbeitah S, Jabareen M, Volokh KY. Dynamic versus quasi-static analysis of crack propagation in soft materials. *J Appl Mech*. 2022;89(12):121008. doi:10.1115/1.4055670
2. Karasudhi P. *Foundations of Solid Mechanics*. 1st ed. Springer; 1991.
3. Madenci E, Oterkus S. Ordinary state-based peridynamics for thermoviscoelastic deformation. *Eng Fract Mech*. 2017;175:31-45. doi:10.1016/j.engfracmech.2017.02.011
4. Volokh KY. *New Approaches to Modeling Failure and Fracture of Rubberlike Materials*. Springer International Publishing; 2021:131-151.
5. Volokh KY. *Mechanics of Soft Materials*. 2nd ed. Springer; 2019.
6. Griffith AA. The phenomena of rupture and flow in solids. *Philos Trans R Soc Lond Ser A Contain Pap Math Phys Character*. 1921;221(582-593):163-198. doi:10.1098/rsta.1921.0006
7. Elishakoff I, Volokh KY. Centenary of two pioneering theories in mechanics. *Math Mech Solids*. 2021;26(12):1896-1904. doi:10.1177/10812865211007552
8. Knauss WG. A review of fracture in viscoelastic materials. *Int J Fract*. 2015;196(1):99-146. doi:10.1007/s10704-015-0058-6
9. Guo J, Zehnder AT, Creton C, Hui CY. Time dependent fracture of soft materials: linear versus nonlinear viscoelasticity. *Soft Matter*. 2020;16(26):6163-6179. doi:10.1039/D0SM00097C
10. Persson BNJ, Brener EA. Crack propagation in viscoelastic solids. *Phys Rev E*. 2005;71(3):036123. doi:10.1103/PhysRevE.71.036123
11. Carbone G, Persson B. Crack motion in viscoelastic solids: the role of the flash temperature. *Eur Phys J E*. 2005;17(3):261-281. doi:10.1140/epje/i2005-10013-y
12. Song SH, Paulino GH, Buttlar WG. A bilinear cohesive zone model tailored for fracture of asphalt concrete considering viscoelastic bulk material. *Eng Fract Mech*. 2006;73(18):2829-2848. doi:10.1016/j.engfracmech.2006.04.030
13. Moes N, Dolbow J, Belytschko T. A finite element method for crack growth without remeshing. *Int J Numer Methods Eng*. 1999;46(1):131-150. doi:10.1002/(SICI)1097-0207(19990910)46:1<131::AID-NME726>3.0.CO;2-J
14. Song JH, Wang H, Belytschko T. A comparative study on finite element methods for dynamic fracture. *Comput Mech*. 2008;42(2):239-250. doi:10.1007/s00466-007-0210-x
15. Fries T, Belytschko T. The extended/generalized finite element method: an overview of the method and its applications. *Int J Numer Methods Eng*. 2010;84(3):253-304. doi:10.1002/nme.2914
16. Wen L, Tian R. Improved XFEM: accurate and robust dynamic crack growth simulation. *Comput Methods Appl Mech Eng*. 2016;308:256-285. doi:10.1016/j.cma.2016.05.013
17. Yu T, Ren Q. Modeling crack in viscoelastic media using the extended finite element method. *Sci China Technol Sci*. 2011;54(6):1599-1606. doi:10.1007/s11431-010-4283-y
18. Ozupek S, Iyidiker C. Computational techniques to predict crack growth in nonlinear viscoelastic materials. *Procedia Struct Integr*. 2016;2:2623-2630. doi:10.1016/j.prostr.2016.06.328
19. Mitchell J. A non-local, ordinary-state-based viscoelasticity model for peridynamics. Sandia National Lab Report 8064; 2011. doi:10.2172/1029821
20. Thamburaja P, Sarah K, Srinivasa A, Reddy J. Fracture of viscoelastic materials: FEM implementation of a non-local and rate form-based finite-deformation constitutive theory. *Comput Methods Appl Mech Eng*. 2019;354:871-903. doi:10.1016/j.cma.2019.05.032
21. Dammas F, Ambati M, Kastner M. A unified phase-field model of fracture in viscoelastic materials. *Contin Mech Thermodyn*. 2021;33(4):1907-1929. doi:10.1007/s00161-021-01013-3
22. Miehe C, Hofacker M, Welschinger F. A phase field model for rate-independent crack propagation: robust algorithmic implementation based on operator splits. *Comput Methods Appl Mech Eng*. 2010;199(45):2765-2778. doi:10.1016/j.cma.2010.04.011
23. Shen R, Waisman H, Guo L. Fracture of viscoelastic solids modeled with a modified phase field method. *Comput Methods Appl Mech Eng*. 2019;346:862-890. doi:10.1016/j.cma.2018.09.018
24. Loew PJ, Peters B, Beex LA. Rate-dependent phase-field damage modeling of rubber and its experimental parameter identification. *J Mech Phys Solids*. 2019;127:266-294. doi:10.1016/j.jmps.2019.03.022
25. Miehe C, Schanzel LM. Phase field modeling of fracture in rubbery polymers. Part I: finite elasticity coupled with brittle failure. *J Mech Phys Solids*. 2014;65:93-113. doi:10.1016/j.jmps.2013.06.007
26. Yin B, Steinke C, Kaliske M. Formulation and implementation of strain rate-dependent fracture toughness in context of the phase-field method. *Int J Numer Methods Eng*. 2020;121(2):233-255. doi:10.1002/nme.6207

27. Brighenti R, Rabczuk T, Zhuang X. Phase field approach for simulating failure of viscoelastic elastomers. *Eur J Mech A Solids*. 2021;85:104092. doi:10.1016/j.euromechsol.2020.104092
28. Zhang X, Vignes C, Sloan SW, Sheng D. Numerical evaluation of the phase-field model for brittle fracture with emphasis on the length scale. *Comput Mech*. 2017;59(5):737-752. doi:10.1007/s00466-017-1373-8
29. Doitrand A, Molnár G, Estevez R, Gravouil A. Strength-based regularization length in phase field fracture. *Theor Appl Fract Mech*. 2023;124:103728. doi:10.1016/j.tafmec.2022.103728
30. Pham K, Marigo JJ. Approche variationnelle de l'endommagement: I. Les concepts fondamentaux. *C R Méc*. 2010;338(4):191-198. doi:10.1016/j.crme.2010.03.009
31. Pham K, Marigo JJ. Approche variationnelle de l'endommagement: II. Les modèles à gradient. *C R Méc*. 2010;338(4):199-206. doi:10.1016/j.crme.2010.03.012
32. Freddi F, Royer-Carfagni G. Regularized variational theories of fracture: a unified approach. *J Mech Phys Solids*. 2010;58(8):1154-1174. doi:10.1016/j.jmps.2010.02.010
33. Pham K, Amor H, Marigo JJ, Maurini C. Gradient damage models and their use to approximate brittle fracture. *Int J Damage Mech*. 2011;20(4):618-652. doi:10.1177/1056789510386852
34. Del Piero G. A variational approach to fracture and other inelastic phenomena. *J Elast*. 2013;112(1):3-77. doi:10.1007/s10659-013-9444-3
35. Volokh KY. Fracture as a material sink. *Mater Theory*. 2017;1(1):3. doi:10.1186/s41313-017-0002-4
36. Faye A, Lev Y, Volokh KY. The effect of local inertia around the crack-tip in dynamic fracture of soft materials. *Mech Soft Mater*. 2019;1(1):4. doi:10.1007/s42558-019-0004-2
37. Abu-Qbeitah S, Jabareen M, Volokh KY. Quasi-static crack propagation in soft materials using the material-sink theory. *Int J Mech Sci*. 2023;248:108160. doi:10.1016/j.ijmecsci.2023.108160
38. Abaqus/CAE, Dassault Systemes Simulia Corp.; 2020.
39. Slootman J, Waltz V, Yeh CJ, et al. Quantifying rate- and temperature-dependent molecular damage in elastomer fracture. *Phys Rev X*. 2020;10:041045. doi:10.1103/PhysRevX.10.041045
40. Marques SPC, Creus GJ. *Computational Viscoelasticity*. 1st ed. Springer; 2012.
41. Aranda-Iglesias D, Vadillo G, Rodríguez-Martínez J, Volokh K. Modeling deformation and failure of elastomers at high strain rates. *Mech Mater*. 2017;104:85-92. doi:10.1016/j.mechmat.2016.10.004
42. Volokh KY. Hyperelasticity with softening for modeling materials failure. *J Mech Phys Solids*. 2007;55(10):2237-2264. doi:10.1016/j.jmps.2007.02.012
43. Volokh KY. On modeling failure of rubber-like materials. *Mech Res Commun*. 2010;37(8):684-689. doi:10.1016/j.mechrescom.2010.10.006
44. Doll S, Schweizerhof K, Hauptmann R, Freischläger C. On volumetric locking of low-order solid and solid-shell elements for finite elastoviscoplastic deformations and selective reduced integration. *Eng Comput*. 2000;17(7):874-902. doi:10.1108/02644400010355871
45. Bishara D, Jabareen M. A reduced mixed finite-element formulation for modeling the viscoelastic response of electro-active polymers at finite deformation. *Math Mech Solids*. 2018;24(5):1578-1610. doi:10.1177/1081286518802419
46. Jabareen M. A polygonal finite element formulation for modeling nearly incompressible materials. *Meccanica*. 2020;55(4):701-723. doi:10.1007/s11012-019-01121-0
47. Weickenmeier J, Jabareen M. Elastic-viscoplastic modeling of soft biological tissues using a mixed finite element formulation based on the relative deformation gradient. *Int J Numer Method Biomed Eng*. 2014;30(11):1238-1262. doi:10.1002/cnm.2654
48. Molnár G, Gravouil A, Seghir R, Réthoré J. An open-source Abaqus implementation of the phase-field method to study the effect of plasticity on the instantaneous fracture toughness in dynamic crack propagation. *Comput Methods Appl Mech Eng*. 2020;365:113004. doi:10.1016/j.cma.2020.113004
49. Newmark NM. A method of computation for structural dynamics. *J Eng Mech Div*. 1959;85(3):67-94. doi:10.1061/JMCEA3.0000098
50. Wilson EL. A computer program for the dynamic stress analysis of underground structures. SESM Report. Department of Civil Engineering, University of California; 1968:68(1).
51. Wilson E, Farhoomand I, Bathe K. Nonlinear dynamic analysis of complex structures. *Earthq Eng Struct Dyn*. 1973;1:241-252.
52. Chung J, Hulbert GM. A time integration algorithm for structural dynamics with improved numerical dissipation: the generalized-α method. *J Appl Mech*. 1993;60(2):371-375. doi:10.1115/1.2900803
53. Hilber H, Hughes T, Taylor R. Improved numerical dissipation for time integration algorithms in structural dynamics. *Earthq Eng Struct Dyn*. 1977;5(3):283-292. doi:10.1002/eqe.4290050306
54. Park K. An improved stiffly stable method for direct integration of nonlinear structural dynamic equations. *J Appl Mech*. 1975;42:464-470.
55. Yin B, Kaliske M. Fracture simulation of viscoelastic polymers by the phase-field method. *Comput Mech*. 2020;65(2):293-309. doi:10.1007/s00466-019-01769-1

How to cite this article: Abu-Qbeitah S, Jabareen M, Volokh KY. Modeling cracks in viscoelastic materials at finite strains. *Int J Numer Methods Eng*. 2023;e7398. doi: 10.1002/nme.7398

APPENDIX A. STRESS AND SPATIAL TANGENT MODULI

To facilitate the reader's understanding of the article, the stress tensor and the spatial tangent moduli are developed in this appendix. The Cauchy stress tensors for springs A and B are computed using $(18)_1$ and $(18)_2$, respectively, which are given by

$$\boldsymbol{\sigma} = \underbrace{\gamma k^{\mathrm{A}}_{\mathrm{bulk}}(J-1)J\mathbf{I} + 2\gamma\left(c^{\mathrm{A}}_1 + 2c^{\mathrm{A}}_2(\eta-3)\right)\mathrm{dev}\mathbf{b}'}_{\boldsymbol{\sigma}_{\mathrm{A}}=2\gamma\frac{\partial W_{\mathrm{A}}}{\partial \mathbf{b}}\mathbf{b}} + \underbrace{\gamma k^{\mathrm{B}}_{\mathrm{bulk}}(J_{\mathrm{B}}-1)J_{\mathrm{B}}\mathbf{I} + 2\gamma\left(c^{\mathrm{B}}_1 + 2c^{\mathrm{B}}_2(\eta_{\mathrm{B}}-3)\right)\mathrm{dev}\mathbf{b}'_{\mathrm{B}}}_{\boldsymbol{\sigma}_{\mathrm{B}}=2\gamma\frac{\partial W_{\mathrm{B}}}{\partial \mathbf{b}_{\mathrm{B}}}\mathbf{b}_{\mathrm{B}}}, \tag{A1}$$

where $\mathbf{b}' = J^{-2/3}\mathbf{b}$ and $\mathbf{b}'_{\mathrm{B}} = J_{\mathrm{B}}^{-2/3}\mathbf{b}_{\mathrm{B}}$ are unimodular tensors. The spatial tangent moduli $\mathbb{a}$, which determines the sensitivity of the stresses with respect to the change of the relative deformation gradient,[47] is given by

$$\mathbb{a} = \frac{1}{J}\frac{\partial \boldsymbol{\tau}}{\partial \mathbf{F}_r}\mathbf{F}_r^{\mathrm{T}} - \boldsymbol{\sigma}\oplus\mathbf{I}, \tag{A2}$$

where $\boldsymbol{\tau} = J\boldsymbol{\sigma}$ is the Kirchhoff stress tensor and the tensor product $\oplus$ is defined as $(\mathbf{A}\oplus\mathbf{B})_{ijkl} = A_{il}B_{jk}$. Substituting (A1) in (A2) yields the following explicit form for the spatial tangent moduli

$$\begin{aligned}\mathbb{a} = {}& \gamma k^{\mathrm{A}}_{\mathrm{bulk}}\left(2J^2 - J\right)\mathbf{I}\otimes\mathbf{I} + 8\gamma c^{\mathrm{A}}_2\mathrm{dev}\mathbf{b}'\otimes\mathrm{dev}\mathbf{b}' + 2\gamma\left(c^{\mathrm{A}}_1 + 2c^{\mathrm{A}}_2(\eta-3)\right)\frac{\partial\,\mathrm{dev}\mathbf{b}'}{\partial\mathbf{F}_r}\mathbf{F}_r^{\mathrm{T}}\\ &+ \gamma k^{\mathrm{B}}_{\mathrm{bulk}}(2J_{\mathrm{B}}-1)\mathbf{I}\otimes\frac{\partial J_{\mathrm{B}}}{\partial\mathbf{F}_r}\mathbf{F}_r^{\mathrm{T}} + 4\gamma c^{\mathrm{B}}_2\mathrm{dev}\mathbf{b}'_{\mathrm{B}}\otimes\frac{\partial\eta_{\mathrm{B}}}{\partial\mathbf{F}_r}\mathbf{F}_r^{\mathrm{T}} + 2\gamma\left(c^{\mathrm{B}}_1 + 2c^{\mathrm{B}}_2(\eta_{\mathrm{B}}-3)\right)\frac{\partial\,\mathrm{dev}\mathbf{b}'_{\mathrm{B}}}{\partial\mathbf{F}_r}\mathbf{F}_r^{\mathrm{T}} - \boldsymbol{\sigma}\oplus\mathbf{I}.\end{aligned} \tag{A3}$$

Using (27) and (31), the derivatives $(\partial J_{\mathrm{B}}/\partial\mathbf{F}_r)\mathbf{F}_r^{\mathrm{T}}$, $(\partial\eta_{\mathrm{B}}/\partial\mathbf{F}_r)\mathbf{F}_r^{\mathrm{T}}$, $\left(\partial\mathrm{dev}\mathbf{b}'/\partial\mathbf{F}_r\right)\mathbf{F}_r^{\mathrm{T}}$, and $\left(\partial\mathrm{dev}\mathbf{b}'_{\mathrm{B}}/\partial\mathbf{F}_r\right)\mathbf{F}_r^{\mathrm{T}}$ are given by

$$\begin{aligned}\frac{\partial J_{\mathrm{B}}}{\partial\mathbf{F}_r}\mathbf{F}_r^{\mathrm{T}} &= \frac{1}{2}J_{\mathrm{B}}\mathbf{b}_{\mathrm{B}}^{-\mathrm{T}} : [\mathbf{I}\ominus\mathbf{b}_{\mathrm{B}} + \mathbf{b}_{\mathrm{B}}\oplus\mathbf{I}],\\ \frac{\partial\eta_{\mathrm{B}}}{\partial\mathbf{F}_r}\mathbf{F}_r^{\mathrm{T}} &= J_{\mathrm{B}}^{-2/3}\mathbf{I} : [\mathbf{I}\ominus\mathbf{b}_{\mathrm{B}} + \mathbf{b}_{\mathrm{B}}\oplus\mathbf{I}] - \frac{1}{3}\eta_{\mathrm{B}}\mathbf{b}_{\mathrm{B}}^{-\mathrm{T}} : [\mathbf{I}\ominus\mathbf{b}_{\mathrm{B}} + \mathbf{b}_{\mathrm{B}}\oplus\mathbf{I}],\\ \frac{\partial\mathrm{dev}\left(\mathbf{b}'\right)}{\partial\mathbf{F}_r}\mathbf{F}_r^{\mathrm{T}} &= \mathbf{b}'\oplus\mathbf{I} + \mathbf{I}\ominus\mathbf{b}' - \frac{2}{3}\mathbf{b}'\otimes\mathbf{I} - \frac{2}{3}\mathbf{I}\otimes\mathbf{b}' + \frac{2}{9}\eta\mathbf{I}\otimes\mathbf{I},\\ \frac{\partial\mathrm{dev}\left(\mathbf{b}'_{\mathrm{B}}\right)}{\partial\mathbf{F}_r}\mathbf{F}_r^{\mathrm{T}} &= \frac{1}{9}\eta_{\mathrm{B}}\mathbf{I}\otimes\left\{\mathbf{b}_{\mathrm{B}}^{-\mathrm{T}} : [\mathbf{I}\ominus\mathbf{b}_{\mathrm{B}} + \mathbf{b}_{\mathrm{B}}\oplus\mathbf{I}]\right\} - \frac{1}{3}\mathbf{I}\otimes\left\{\mathbf{I} : \left[\mathbf{I}\ominus\mathbf{b}'_{\mathrm{B}} + \mathbf{b}'_{\mathrm{B}}\oplus\mathbf{I}\right]\right\}\\ &\quad - \frac{1}{3}\mathbf{b}_{\mathrm{B}}\otimes\left\{\mathbf{b}_{\mathrm{B}}^{-\mathrm{T}} : \left[\mathbf{I}\ominus\mathbf{b}'_{\mathrm{B}} + \mathbf{b}'_{\mathrm{B}}\oplus\mathbf{I}\right]\right\} + \mathbf{I}\ominus\mathbf{b}'_{\mathrm{B}} + \mathbf{b}'_{\mathrm{B}}\oplus\mathbf{I},\end{aligned} \tag{A4}$$

where the tensor product $\ominus$ is defined as $(\mathbf{A}\ominus\mathbf{B})_{ijkl} = A_{ik}B_{jl}$.

APPENDIX B. IMPLEMENTATION ASPECTS

The developed mixed finite-element formulation based on the relative deformation gradient is implemented in the commercial finite-element software Abaqus/Standard 2020. The user-defined element utility provided by Abaqus software is employed, where the formulation has been implemented by means of a UEL subroutine. The UEL is a general user-defined element provided by Abaqus/Standard that is called for each element at each time-increment. It has to perform all the calculations for the user-defined element and provide the residual vector (RHS) and stiffness matrix (AMATRX) back to Abaqus.

The coupled system of displacements and relative mass density is solved based on the staggered solution technique. In the staggered scheme, the two fields—displacement and relative density—are separated. In each iteration, both fields are solved separately based on the values calculated from the previous iteration. Thus, the displacement field is calculated primarily from the momentum balance based on the relative density values calculated from the previous iteration. Likewise, the relative density is calculated primarily by solving the mass balance based on the displacement values calculated from the previous iteration.

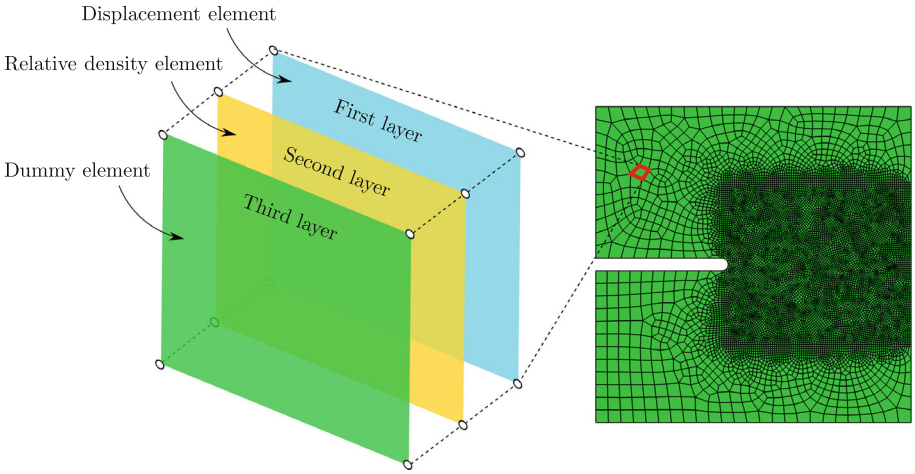

FIGURE B1 Representation of three layers finite elements structure in Abaqus. The first and second layers contribute to the stiffness of the displacement DOFs and relative density DOF, accordingly, created as UEL models. For visualization, a third layer created as a UMAT model, with no stiffness, overlies the first two layers.

Three layers[§] of elements are created in Abaqus as depicted in Figure B1. The first two layers solve the coupling problem, while the third layer is created to visualize the results from the first two layers. The first layer solves for the displacement field, while the second layer solves for the relative density field. Namely, in the two-dimensional case, a four-node quadrilateral element is used with two displacement degrees of freedom for each node defined for the first layer, while a relative density degree of freedom for each node is defined for the second layer. In the three-dimensional case, an eight-node brick element is used with three displacement degrees of freedom for each node defined for the first layer, while a relative density degree of freedom for each node is defined for the second layer, where the temperature degree of freedom is used to store the relative density. The latter analogy can be used to define any additional scalar degree of freedom that is not provided explicitly by the Abaqus built-in solver. As already mentioned, the first two layers are implemented using the user-defined element utility UEL. However, a difficulty associated with using user-defined element subroutines from Abaqus is that the results cannot be visualized since the element's shape functions are defined by the user. This drawback can be bypassed by using a dummy mesh with negligible stiffness laying over the user-defined elements. It is important that the dummy mesh should be created from Abaqus built-in elements that have the same number of nodes and integration points as the user-defined elements. Thus, the third layer is created using the user-defined material subroutine UMAT that is also employed to transfer information from the common block.

First, regarding implementing the first layer (i.e., the displacement element), the detailed steps are described in the following flowchart:

- Loop over the Gauss points
  - o Compute the shape functions and their derivatives with respect to the current configuration.
  - o Compute the deformation gradient, $\mathbf{F} = \left(\mathbf{I} - \sum_{I=1}^{n_{en}} \hat{\mathbf{u}}^I \otimes \frac{\partial N_I}{\partial \mathbf{x}}\right)^{-1}$ and $J = \det(\mathbf{F})$.
  - o Compute the relative deformation gradient $\mathbf{F}_r = \left(\mathbf{I} - \sum_{I=1}^{n_{en}} \Delta\hat{\mathbf{u}}^I \otimes \frac{\partial N_I}{\partial \mathbf{x}}\right)^{-1}$ and $J_r = \det(\mathbf{F}_r)$.
  - o Compute the deformation gradient at time t_n, $\mathbf{F}^n = \mathbf{F}_r^{-1}\mathbf{F}$, and $J^n = \det\left(\mathbf{F}^n\right)$.
  - o Compute the B-matrix as in (45).
- Compute the relative volume average of the dilatation $\bar{J}_r$ using $(40)_1$, $\bar{J}$, and $\bar{J}^n$.
- Loop over the Gauss points
  - o Compute the modified relative deformation gradient $\widetilde{\mathbf{F}}_r$ using $(36)_2$.
  - o Compute the modified left Cauchy–Green tensor $\widetilde{\mathbf{b}}$ using $(39)_1$, and the modified deformation tensor in spring B ($\widetilde{\mathbf{b}}_{\mathrm{B}}$) using $(39)_2$.
  - o Compute the Cauchy stress tensor in branch A ($\widetilde{\boldsymbol{\sigma}}_{\mathrm{A}}$) using $(18)_1$, where $\widetilde{\mathbf{b}}$ is used instead of $\mathbf{b}$.
  - o Compute the Cauchy stress tensor in branch B ($\widetilde{\boldsymbol{\sigma}}_{\mathrm{B}}$) using $(18)_2$, where $\widetilde{\mathbf{b}}_{\mathrm{B}}$ is used instead of $\mathbf{b}_{\mathrm{B}}$.

- Compute $\widetilde{\mathbf{d}}_{\mathrm{B}}$ using $(21)_2$, where $\widetilde{\boldsymbol{\sigma}}_{\mathrm{B}}$ is used instead of $\boldsymbol{\sigma}_{\mathrm{B}}$.
- Compute the total Cauchy stress $\widetilde{\boldsymbol{\sigma}} = \widetilde{\boldsymbol{\sigma}}_{\mathrm{A}} + \widetilde{\boldsymbol{\sigma}}_{\mathrm{B}}$.
- Compute $\widetilde{p}$ using $(38)_2$.
- Compute the spatial tangent moduli using (A2), where $\widetilde{\mathbf{b}}$ is used instead of $\mathbf{b}$ and $\widetilde{\mathbf{b}}_{\mathrm{B}}$ is used instead of $\mathbf{b}_{\mathrm{B}}$.

- Compute the average hydrostatic pressure within the element domain $\overline{p}$ using $(40)_2$.
- Loop over the Gauss points
  - Compute the modified Cauchy stress tensor $\widetilde{\widetilde{\boldsymbol{\sigma}}}$ using $(38)_1$.
  - Compute the fourth-order tensor $\widetilde{\mathbb{a}}_{uu}$, the second-order tensors $\left\{\widetilde{\mathbf{a}}_{u\bar{J}_r}, \widetilde{\mathbf{a}}_{\bar{J}_r u}\right\}$, and the scalar $\widetilde{\alpha}_{\bar{J}_r\bar{J}_r}$ using (42).
- Compute the tangent stiffness matrix using (51).
- Compute the nodal internal forces using $(47)_2$.

Second, regarding implementing the second layer (i.e., the relative density element), the detailed steps are described as follows:

- Loop over the Gauss points
  - Compute the shape functions and their derivatives with respect to the current configuration.
  - Compute the relative mass density field using $(54)_1$.
  - Compute $\underline{\mathbf{N}}_{\gamma}$ (i.e., $\underline{\mathbf{N}}_{\gamma} = \{N_1,\ N_2,\ \ldots, N_{n_{en}}\}$) and $\underline{\underline{\mathbf{B}}}_{\gamma}$ using $(56)_2$.
  - Compute $\widetilde{\mathbf{f}}$ and $\widetilde{\zeta}$ using $(14)_1$ and (16), respectively, where the modified left Cauchy–Green deformation tensor is used instead of the left Cauchy–Green deformation tensor.
  - Compute the moduli $\widetilde{\mathbf{C}}_{\gamma\gamma}$ and $\widetilde{\mathrm{C}}_{\gamma\gamma}$ using (60).
- Compute the stiffness matrix using (61).
- Compute the nodal internal forces using (58).

Finally, there are two tips regarding writing the input file. Based on the author's experience, it is recommended to suppress any extrapolation in the step by setting EXTRAPOLATION=NO. The latter note is highly important when modeling cracks, since in some cases extrapolation may cause Abaqus to iterate unreasonably. One common example of such behavior is the abrupt change in the load magnitude or the boundary conditions and if unloading occurs as a result of cracking or buckling.[38] Further, since a large deformation is considered, it is important to include the changes in geometry during the analysis. Thus, the NLGEOM keyword should be turned on by setting NLGEOM=YES. This indicates to Abaqus that geometric nonlinearity should be accounted for during the step.[38]

APPENDIX C. GENERALIZATION OF THE VISCOELASTIC MODEL TO A NUMBER OF DASHPOT-SPRING ELEMENTS

The described constitutive model of the "standard solid" can be readily generalized based on the rheological model shown in Figure C1, which is a combination of the spring element and multiple parallel spring-dashpot elements. Now, the subscript B is replaced by index B whose value runs from $B = 1$ to $B = N$. The evolution equation of the deformation measure $\mathbf{b}_B$ in each spring $B = 1, \ldots, N$ is given by

$$\dot{\mathbf{b}}_B = (\mathbf{1} - \mathbf{d}_B)\mathbf{b}_B + \mathbf{b}_B(\mathbf{1} - \mathbf{d}_B)^{\mathrm{T}}, \quad (B = 1, \ldots, N), \tag{C1}$$

and the Helmholtz free energy per unit mass w is decomposed as follows

$$w(\mathbf{b}, \mathbf{b}_B) = w_A(\mathbf{b}) + \sum_{B=1}^{N} w_B(\mathbf{b}_B). \tag{C2}$$

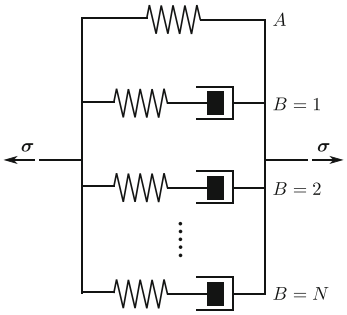

FIGURE C1 Generalized rheological model of the viscoelastic solid.

In this contribution, we ignore thermal processes and we use the dissipation inequality in the reduced form

$$D_{\text{int}} = \underbrace{\left(\boldsymbol{\sigma}_A + \sum_{B=1}^{N} \boldsymbol{\sigma}_B\right)}_{\boldsymbol{\sigma}} : \mathbf{d} - \varrho \dot{w} \geq 0. \tag{C3}$$

Substituting the time derivative of the strain energy function (C2) into the dissipation inequality (C3), using the evolution Equations (5) and (C1), and noting the symmetry feature defined in (9), the constitutive laws for springs A and B are, respectively, given by

$$\boldsymbol{\sigma}_A = 2\varrho \frac{\partial w_A}{\partial \mathbf{b}} \mathbf{b}, \quad \boldsymbol{\sigma}_B = 2\varrho \frac{\partial w_B}{\partial \mathbf{b}_B} \mathbf{b}_B, \quad (B = 1, \ldots, N), \tag{C4}$$

and the dissipation inequality reduces to

$$D_{\text{int}} = \sum_{B=1}^{N} \boldsymbol{\sigma}_B : \mathbf{d}_B \geq 0. \tag{C5}$$

The flow rule for dashpot $B = 1, \ldots, N$ can be written in the following general form

$$\boldsymbol{\sigma}_B = \beta_1^{(B)} \mathbf{I} + \beta_2^{(B)} \mathbf{d}_B + \beta_3^{(B)} \mathbf{d}_B^2, \quad (B = 1, \ldots, N), \tag{C6}$$

where $\beta_j^{(B)}$ is a function(al), generally, depending on stresses and strains. Substituting the flow rule (C6) in the latter inequality we get the final thermodynamic restriction

$$D_{\text{int}} = \sum_{B=1}^{N} \left(\beta_1^{(B)} \text{tr}\mathbf{d}_B + \beta_2^{(B)} \text{tr}\mathbf{d}_B^2 + \beta_3^{(B)} \text{tr}\mathbf{d}_B^3\right) \geq 0. \tag{C7}$$